

## ABSTRACT

Title of Thesis: EIT BASED PIEZORESISTIVE TACTILE  
SENSORS: A SIMULATION STUDY

Ayush Nankani

Master of Science, 2019

Thesis Directed By: Professor Elisabeth Smela  
Department of Mechanical Engineering

Electrical impedance tomography (EIT) is an imaging technique that uses voltage measurements to map the internal conductivity distribution of a body by applying current on electrodes attached to the boundary of that body. EIT has many applications, ranging from medical imaging to 3D printing. This imaging method is also being used for tactile sensing using stretchable piezoresistive sensors, mainly for robotic applications. Although prior research has focused on qualitative illustrations of tactile sensing, this thesis focuses on quantitative evaluation. In this thesis different current injection patterns are quantitatively analyzed using performance metrics to understand their effect on the resulting EIT images.

EIT BASED PIEZORESISTIVE TACTILE SENSORS: A SIMULATION STUDY

by

Ayush Nankani

Thesis submitted to the Faculty of the Graduate School of the  
University of Maryland, College Park, in partial fulfillment  
of the requirements for the degree of  
Master of Science  
2019

Advisory Committee:

Dr. Elisabeth Smela, Chair/Advisor

Dr. Miao Yu

Dr. Nikhil Chopra

## **Acknowledgements**

I owe my gratitude to all the people who have made this thesis possible and because of whom my graduate experience has been one that I will cherish forever.

First, I would like to express my sincere gratitude to my advisor Professor Elisabeth Smela for the continuous support during my research study, for her patience, motivation, enthusiasm, and immense knowledge. I would also like to thank her for giving me an invaluable opportunity to work on interesting and challenging projects, which will help people in the future. Her guidance helped me in all the time of research and writing of this thesis. I could not have imagined having a better advisor and mentor for my research study. I would also like to thank Prof. Miao Yu and Prof. Hugh A. Bruck for consistently providing me valuable advice and immediate help. I am also very thankful to Prof. Nikhil Chopra, who was very generous to agree to serve on my committee.

I would like to acknowledge the support received the Clark School's 125th Anniversary Challenge. I am very thankful to all my colleagues in Laboratory for Microtechnologies, Dr. Ahmed Ramadan for providing me valuable advice; Dr. Ying Chen for helping me in my research; Hudson, Shirley, Rahul, Ajeet, Likhita, Meghana for always supporting and helping me during my research. Finally yet importantly, I would like to thank my family for supporting throughout my life.

# Table of Contents

Acknowledgements.....	ii
Table of Contents.....	iii
List of Figures.....	v
Chapter 1. Introduction.....	1
1.1 Background and Motivation.....	1
1.2 Electrical Impedance Tomography (EIT) .....	1
1.3 EIT based tactile sensing.....	3
1.4 EIDORS .....	5
Chapter 2. Quantitative Evaluation of EIT Current Injection Patterns for Tactile Sensing: A Simulation Study.....	7
Abstract.....	7
2.1 Introduction .....	8
2.1.1 Measured Data .....	10
2.1.2 Performance Metrics.....	14
2.2 Methods.....	16
2.3 Results and Discussion.....	17
2.3.1 Comparison of Injection Patterns in Noise-Free Simulations.....	17
2.3.2 Comparison of Injection Patterns with Noise .....	24
2.3.3 Effect of a Larger Hyperparameter .....	26
2.4 Conclusions .....	33

Chapter 3. Concluding Remarks and Future Work .....	34
Appendix A. MATLAB Code.....	36
Appendix B: Supporting Information for Chapter 2.....	56
Bibliography .....	62

## List of Figures

Figure 1.1 Stretchable single-layered EIT-based artificial skin. (a) Square of artificial skin placed over a complex three-dimensional surface. (b) Pressure applied over the artificial skin. (c) Two-dimensional representation of the reconstructed conductivity changes due to pressure applied at the locations represented by the white circles in (b). [6, 12]

Figure 1.2 Demonstration of (top row) a) single-point, b) two-point, and c) three point finger presses, and d) a light fist-punch, together with (center row) EIT images, where  $d_s$  represents the conductivity change. (e) Demonstration of finger sliding from left to right and EIT images recorded at different times ( $t = 1.0, 1.6,$  and  $2.2$  sec) during similar finger sliding. [13]

Figure 1.3 Image reconstruction of sensor experiencing a single touch using difference EIT in EIDORS. The difference of voltage measurements from a sensor with ( $\vec{V}_{touch}$ ) and without ( $\vec{V}_{ref}$ ) a target or touch (blue) is used to reconstruct the EIT image.

Figure 2.1. a) Schematic showing the three most commonly discussed injection patterns: adjacent, pseudo-polar, and polar. The x symbols indicate pairs of electrodes between which voltages are not recorded. b) Calculated voltage across the injecting electrodes as a function of the position of the current injection electrode, with ground

kept at electrode 1 (constant 3 mA injection current, uniform baseline  $\sigma_0 = 0.01$  S/m).  
c) Simulated equipotential lines in the reference image for the adjacent injection pattern for a membrane of constant baseline conductivity  $\sigma_0$ . d) Equipotential lines in the reference image for the pseudo-polar pattern (yellow shows the maximum of 0.9 V to blue shows the minimum of 0 V with intervals of 0.07 V).

Figure 2.2. a) Boundary potentials  $\vec{V}_{touch}$  and  $\vec{V}_{ref}$  resulting from ADJ with (red) and without (black) a touch near the perimeter ( $x = 0.7$ ), respectively. b) The signal  $\Delta = \vec{V}_{touch} - \vec{V}_{ref}$  (thin line), the absolute value of  $\Delta$  (thick line), and the average of the signal  $\Delta$  (dashed line). c) For PP,  $|\Delta|$  and the mean of  $|\Delta|$ . Note the change in scale.

Figure 2.3. The metrics used to evaluate the reconstructions. a) A circular membrane with 16 electrodes at the boundary illustrating an original target stimulus at  $x = 0.5$  with radius  $r_t = 0.2$ , area  $A_0$ , and b) constant amplitude  $\Delta\sigma$  and c) the reconstructed image of a target with amplitude  $A$  and area  $A_R$ , defined as the region having values greater than the FWQM. The d) size, c) position, and e) shape errors.

Figure 2.4 EIT images reconstructed from noise free simulation data of targets positioned at various positions along the  $x$ -axis for a) adjacent b) pseudo-polar c) polar current injection patterns. The color indicates the amplitude of the reconstructed  $\Delta\sigma$  at each position. ( $\lambda = 4 \times 10^{-8}$ ,  $\sigma_0 = 0.01$  S/m,  $\Delta\sigma = 4$  mS/m).

Figure 2.5 Cross-sections taken along the  $x$ -axis of the reconstructed EIT images of Figure 2.4 showing amplitude as a function of the target position for a) adjacent b) pseudo-polar c) polar current injection patterns. Black lines indicate positions  $x = 0$  and  $0.7$ , gray lines show intermediate positions, and dashed lines show  $x = 0.8$  and  $0.9$ . Points indicate the maximum values.

Figure 2.6 Performance metrics for the three current injection patterns for the noise-free case ( $\lambda = 4 \times 10^{-8}$ ,  $\sigma_0 = 0.01$  S/m,  $\Delta\sigma = 4$  mS/m): a) size error, b) position error, and c) shape error vs  $x$ -position.

Figure 2.7. Reconstructed images for a target at  $x = 0$  with  $3 \times 10^{-4}$  V of noise with a hyperparameter of  $\lambda = 2 \times 10^{-2}$  for a) adjacent (SNR = 3 dB) and b) pseudo polar (SNR = 12 dB) injections. c) For the same hyperparameter, the reconstruction for the adjacent pattern for a target at  $x = 0.7$  (SNR = 10 dB).

Figure 2.8 EIT images reconstructed from noise-free simulation data with a larger hyperparameter,  $\lambda = 2 \times 10^{-2}$ , for the target at different positions for a) adjacent, b) pseudo-polar, and c) polar current injection patterns. ( $\sigma_0 = 0.01$  S/m,  $\Delta\sigma = 4$  mS/m).

Figure 2.9 Cross-sections along the  $x$ -axis of the reconstructed EIT images in Figure 2.8 showing amplitude as function of the target position for a) adjacent b) pseudo-polar c) polar current injection pattern.

B 1 TOP: Boundary potentials  $\vec{V}_{touch}$  and  $\vec{V}_{ref}$  resulting from PP with (orange) and without (blue) a touch near the perimeter ( $x = 0.7$ ), respectively. BOTTOM: The signal

$$\Delta = \vec{V}_{touch} - \vec{V}_{ref}. \text{ Note the negative values.}$$

B 2 Cross-section profiles with different targets sizes (from  $r_t = 0.2$  to  $0.9$ ) with  $\Delta\sigma = 0.001$  (top left),  $\Delta\sigma = 0.004$  (top right),  $\Delta\sigma = 0.009$  (bottom left),  $\Delta\sigma = 0.0099$  S/m (bottom right).

B 3 Amplitude as a function of  $\Delta\sigma$  with  $\sigma_0 = 0.01$  S/m

B 4 Amplitude as a function of change in resistivity with baseline resistivity  $\rho = 100$  ohm-m ( $\sigma = 0.01$  S/m).

B 5 Hyperparameter vs (a) Amplitude (b) Reconstructed size (c) Position Error (d) Shape error with target at  $x = 0$  (blue) and  $x = 0.7$  (orange).

B 6 Reconstructed EIT images with polar injection pattern with different hyperparameter. Reconstruction failed below  $\lambda = 4 \times 10^{-8}$ . Note change in scale with different hyperparameter.

B 7 (Top row) Reconstructed images for a target at  $x = 0$  and  $x = 0.7$  (Center row) with  $3 \times 10^{-4}$  V with a hyperparameter of  $\lambda = 2 \times 10^{-2}$  for adjacent injection. (Bottom row)

Reconstructed images for a target at  $x = 0$  with  $3 \times 10^{-4}$  V with a hyperparameter of  $\lambda = 2 \times 10^{-2}$  pseudo polar injection.

# **Chapter 1. Introduction**

## **1.1 Background and Motivation**

EIT was mainly developed for medical applications; therefore, a lot of research has been done to obtain qualitative data for those applications [1-3]. Recent studies have focused on other applications of EIT, like artificial stretchable skins for robotic applications [4-6], which would be useful for establishing human-robot communication.

This thesis aims to understand the effect of different current injection patterns on quantitative information from piezoresistive tactile sensors using EIT. This study will help the research being carried out in the Laboratory for Microtechnologies at the University of Maryland, which involves using the same piezoresistive sensors for developing a wearable device to detect breast cancer.

## **1.2 Electrical Impedance Tomography (EIT)**

Electrical impedance tomography is an imaging technique that uses current injection and voltage measurements at electrodes at the surface to determine the impedance within a body. It was initially used for clinical applications such as cardiac imaging or breast cancer detection [2].

There are two types of problems in EIT, namely forward and inverse problems. The forward problem refers to calculating potentials at the electrodes when the conductivity inside the body is known. If a given body  $\Omega$ , with a closed smooth boundary  $\partial\Omega$  has a conductivity  $\sigma$ , the potential is  $\varphi$  and electric field is  $\mathbf{E} = -\nabla\varphi$ . Then, according to Ohm's Law the current density is  $\mathbf{J} = -\sigma\nabla\varphi$ . And according to Kirchhoff's Law, in the absence of interior current sources the voltage distribution can be determined by Laplace's equation:

$$(1) \quad \nabla \cdot \sigma \nabla \varphi = 0$$

Inverse problem refers to determining the internal conductivity distribution using the boundary voltages. In all but the simplest of cases, this inversion is an ill-posed problem [2] with more unknown parameters than known measurements (i.e. there are fewer voltage measurements than positions within the body). This ill-posed problem, as defined by Hadamard [2], fails to adhere to one of the following properties, that small changes in the data result in small changes in the solution. The one-step Gauss-Newton method [7] is used for solving the nonlinear inverse problem. The objective of this approach is to minimize the difference between the measured electric voltages on the electrodes and voltage based on an estimation of conductivity.

$$(2) \quad \min \|V - F(\sigma)\|^2$$

where  $\|\cdot\|^2$  is the norm and  $V$  is voltage measured at the boundary.  $F(\sigma)$  is a forward operator, converting conductivity to voltages.

Due to its ill-posed nature, a regularization term is introduced to the minimization function to make it well-posed. After regularization, the objective function becomes:

$$(3) \quad \min (\|V - F(\sigma)\|^2 + \lambda\|\sigma - \sigma_0\|^2)$$

where  $\lambda$  is referred to as the hyperparameter. By selecting a proper value of the hyperparameter the ill-posed nature of the inverse problem can be alleviated. There are many different algorithms [7-11] that can be used to solve this type of inverse problem.

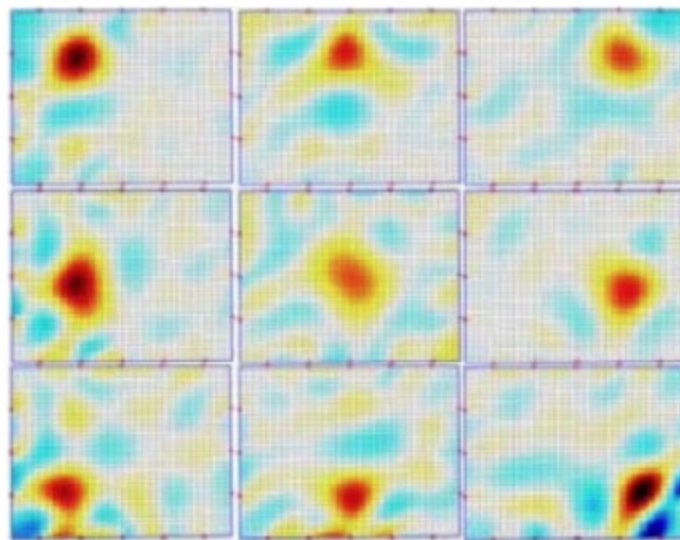
### **1.3 EIT based tactile sensing**

EIT was employed in tactile sensing for the first time during the 2000s [6]. An example of a tactile sensor [6, 12] used for human-robot interaction is shown in Figure 1.1.



(a) Stretchable artificial skin.

(b) Points of pressure.



(c) 2-D representation of conductivity changes.

**Figure 1.1 Stretchable single-layered EIT-based artificial skin. (a) Square of artificial skin placed over a complex three-dimensional surface. (b) Pressure applied over the artificial skin. (c) Two-dimensional representation of the reconstructed conductivity changes due to pressure applied at the locations represented by the white circles in (b). [6, 12]**

One advantage of EIT is that quantitative information on target/touch can be known from the reconstructed image: positions, intensity, and contact area. Multiple touch points over planar or curved surfaces can be detected. A variety of sensing materials can be used for manufacturing EIT tactile sensors, such as carbon filled elastomers, conductive fabric, and ionic liquids. Figure 1.2 shows different types of touch detected using a stretchable piezoresistive sensor [13].

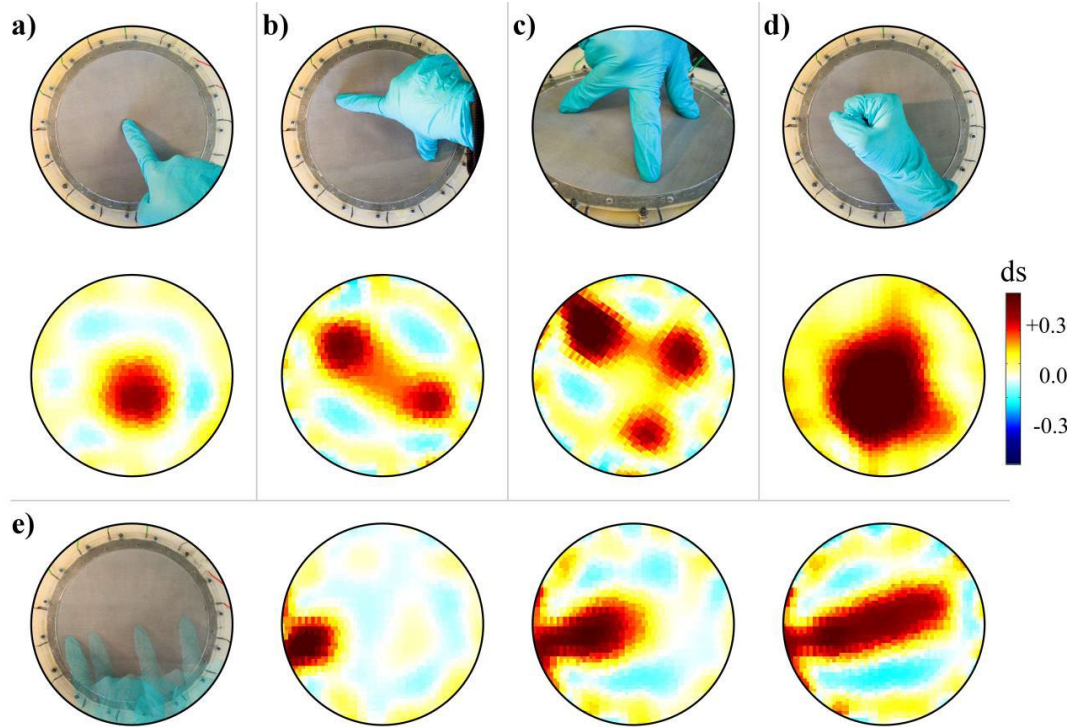


**Figure 1.2 Demonstration of (top row) a) single-point, b) two-point, and c) three point finger presses, and d) a light fist-punch, together with (center row) EIT images, where  $ds$  represents the conductivity change. (e) Demonstration of finger sliding from left to right and EIT images recorded at different times ( $t = 1.0, 1.6,$  and  $2.2$  sec) during similar finger sliding. [13]**

#### 1.4 EIDORS

EIDORS [14-16] is an open source software, which is implemented in MATLAB, to solve both forward and inverse EIT problems. EIDORS, along with Netgen (a meshing software), is used to reconstruct EIT images using simulated or experimental data with different methods and algorithms. In this thesis, only static, time-independent EIT problems were considered. EIDORS can also be used for a time variant problems. Figure 1.3 shows a typical flow diagram involving forward and reverse problem in EIDORS.

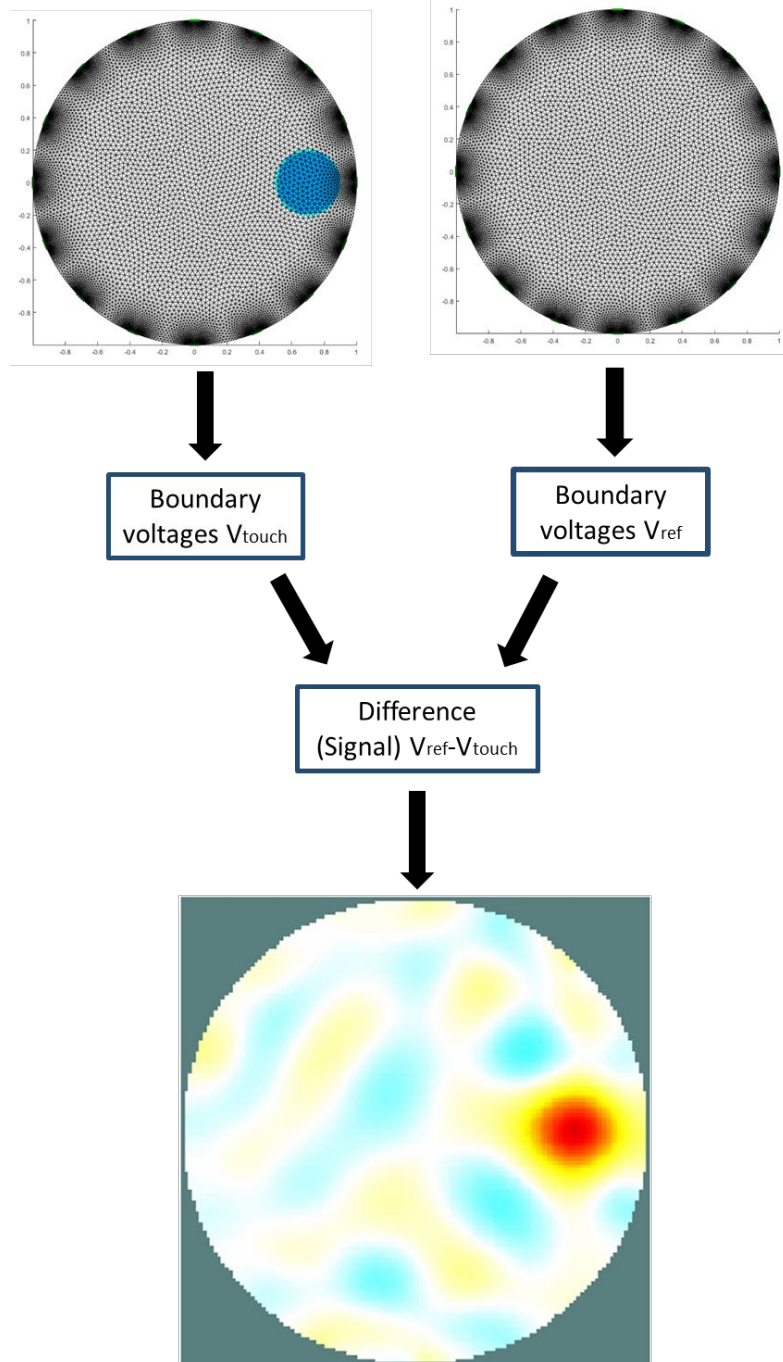


**Figure 1.3** Image reconstruction of sensor experiencing a single touch using difference EIT in EIDORS. The difference of voltage measurements from a sensor with ( $\vec{V}_{touch}$ ) and without ( $\vec{V}_{ref}$ ) a target or touch (blue) is used to reconstruct the EIT image.

## **Chapter 2. Quantitative Evaluation of EIT Current Injection**

### **Patterns for Tactile Sensing: A Simulation Study**

This chapter consists of a draft in preparation for a journal publication (for example in IEEE Sensors Journal). **Co-author contributions:** The idea of quantitatively analyzing EIT tactile sensing comes from the discussion among authors. Ayush Nankani conducted simulations and analyzed the data under the guidance of E. Smela. Both authors contributed to writing the text and making the figures.

#### **Abstract**

This paper quantitatively analyzes the effects of several commonly used current injection patterns on reconstructed electrical impedance tomography images using simulations. The simulations were performed using the open source software EIDORS (Electrical Impedance Tomography and Diffuse Optical Tomography Reconstruction Software). Performance evaluation for different current injection patterns was done using performance metrics like amplitude, errors (position, shape, and size), signal-to-noise ratio (SNR) and volume under the curve. For a fixed current injection, polar and ‘pseudo-polar pattern’ yield the highest voltage readings due to higher resistance between the driving electrodes and therefore give the highest SNR. For all other performance parameters, the differences between the patterns was small, except for the “polar” pattern, which performed poorly. Thus, the pseudo-polar pattern should be used to minimize power consumption.

## 2.1 Introduction

Tomography refers to imaging the internal properties of a body from measurements made on its surface by using penetrating electromagnetic energy. Electrical impedance tomography (EIT) is a technique for mapping the internal conductivity distribution of a body using current injection and voltage measurements made at the perimeter. EIT was developed for medical imaging [2] and has recently been adapted for use in piezoresistive [4, 6, 12, 17] and capacitive [6] tactile sensing, among other applications [18, 19]. The terms electrical resistance tomography (ERT) and electrical resistivity imaging (ERI) are also used when the current is DC.

To obtain boundary voltage data, a current is injected at one pair of electrodes and voltages are measured between the others (See Figure 2.1(a)). Typically 16 electrodes are used [6, 12, 20-22]. There are various voltages measurement patterns, but the dominant pattern used is the “adjacent” pattern [22, 23], in which voltage differences between neighboring electrodes are obtained. (In practice the voltages may be recorded between each electrode and ground, and the differences between adjacent electrodes calculated in software.) Various electrode pairs can be used to inject the current [23]. In the adjacent injection pattern the current-injecting electrodes are also immediate neighbors, such as electrodes 1 and 2, whereas in the “polar” pattern they are on opposite sides of the membrane (i.e. electrodes 1 and 9). Voltages are not recorded between injecting electrodes and their immediate neighbors, as indicated in Figure 2.1(a), so 13 voltage differences are obtained for the adjacent injection pattern and 12 for the others. The injection electrodes are then rotated to the next position (e.g. to

electrodes 2 and 3 for adjacent, 2 and 10 for polar), and voltages are again obtained between the other electrodes. The process continues around the circle; in the adjacent pattern this leads to a total of  $16 \times 13 = 208$  voltage measurements. Other injection patterns, such as the trigonometric, have also been proposed [5], but the hardware complexity required for implementation means that they are rarely used, so we do not treat them here.

There has been discussion concerning the benefits of the various injection patterns [22, 23], particularly the adjacent (ADJ), polar (P), and pseudo-polar (PP) [24] injection patterns (Figure 2.1(a)). It has been found that the pseudo-polar pattern produces greater detectability of conductivity changes and therefore allows use of a smaller injection current for medical imaging [23]. Others have recommended using a combination of patterns to take advantage of difference sensitivities at the center and the edges of the sensing area [22]. However, quantitative comparisons have been missing, of the performance of different injection patterns. This paper for the first time quantitatively examines the performance of the most frequently used current injection patterns using simulations.

The usual definition of signal to noise ratio (SNR) is the mean of the signal divided by the standard deviation of the signal. However, in difference EIT the signal is  $\Delta$ , which is a series of correlated voltages of different amplitude, depending on the electrode position relative to the current injection site and the stimulus. The variations in  $\Delta$  are not noise. To obtain the noise, the variation in the measured voltages at a single

electrode are made over time. In our lab, we have found the standard deviation of the noise to be approximately 0.3 mV [4]. In this paper, we adopted the usual assumption of normally distributed (white) noise independent of the measured voltage, which may or may not be the case for a given experimental pattern.

### 2.1.1 Measured Data

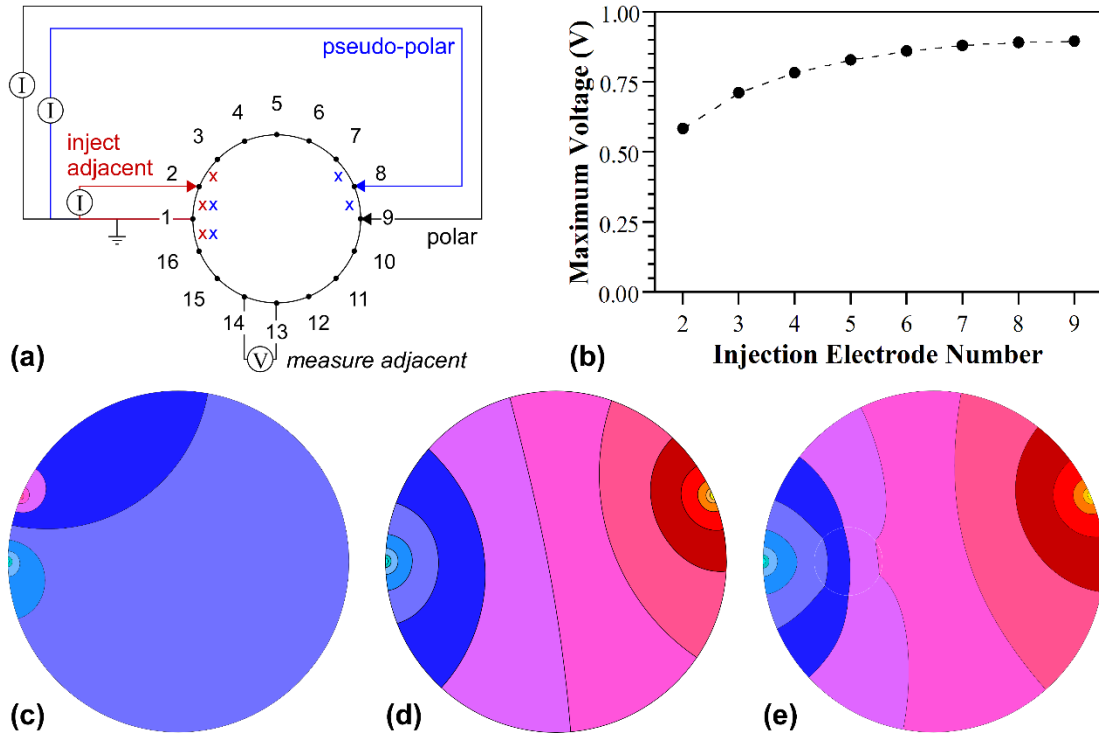


**Figure 2.1.** a) Schematic showing the three most commonly discussed injection patterns: adjacent, pseudo-polar, and polar. The x symbols indicate pairs of electrodes between which voltages are not recorded. b) Calculated voltage across the injecting electrodes as a function of the position of the current injection electrode, with ground kept at electrode 1 (constant 3 mA injection current, uniform baseline  $\sigma_0 = 0.01$  S/m). c) Simulated equipotential lines in the reference image for the adjacent injection pattern for a membrane of constant baseline conductivity  $\sigma_0$ . d) Equipotential lines in the reference image for the pseudo-polar pattern (yellow shows the maximum of 0.9 V to blue shows the minimum of 0 V with intervals of 0.07 V).

For a constant injection current, the voltage between the injecting electrodes is higher the further apart they are, since  $V = IR$ . Figure 2.1(b) shows the voltage difference for

a current of 3 mA and a baseline conductivity of  $\sigma_0 = 0.01$  S/m. The simulation results agree with a calculation of the resistance between points on a resistive circular area. Thus, the measured EIT voltages are highest for the polar pattern. For a fixed amount of noise, this would give the highest signal to noise ratio (SNR).

Simulated equipotential lines are shown in Figure 2.1(c) for the adjacent injection pattern and Figure 2.1(d) the pseudo-polar pattern with uniform conductivity, and for Figure 2.1(e) the pseudo-polar with a circular area having a different conductivity than the background, indicated by the dashed line. The equipotential lines are distorted by the change in  $\sigma$ . As seen in Figure 2.1(b) the voltage drop between the current injecting electrodes is larger for the pseudo-polar pattern. To obtain an image of a conductivity change, such as due to a touch on a tactile sensor, the conductivity within the sensing area is compared to a reference image, which for tactile sensing is typically one obtained without a touch (Figure 2.1(c) and (d)).

Figure 2.2(a) shows the 208 voltage differences in  $\vec{V}_{touch}$  and  $\vec{V}_{ref}$  resulting from the adjacent pattern. The voltage differences are highest near the injection electrode and decrease with distance, resulting in a series of  $U_s$ , as shown in Figure 2.2(a). For the pseudo-polar pattern, there are regions where the differences are negative (see SI Figure B 1). The two voltage vectors  $\vec{V}_{touch}$  and  $\vec{V}_{ref}$  are subtracted, giving a “differences of differences” array,  $\Delta = \vec{V}_{touch} - \vec{V}_{ref}$  (Figure 2.2(b)), which is the signal that is input to the EIT algorithm. The average amplitude of the signal is obtained from the absolute

values of  $\Delta$ . The pattern in Figure 2.2 (b) resulted from touch near the edge of the membrane; the pattern changes with the location of the touch. The values in  $\Delta$  are small, with maxima of approximately 10 mV for the adjacent injection pattern with an injection current of 3 mA, a membrane with baseline conductivity 0.01 S/m, and a conductivity difference of 0.004 S/m. The voltage differences in  $\Delta$  increase with the size of the stimulus, i.e. the strength of the touch. The values of  $\Delta$  for the pseudo-polar injection pattern are a factor of around 2.5 larger, as expected from Figure 2.1(e). The plot also shows that there are fewer values (192) in  $\Delta$  for the pseudo-polar injection pattern (as compared to 208 in adjacent).

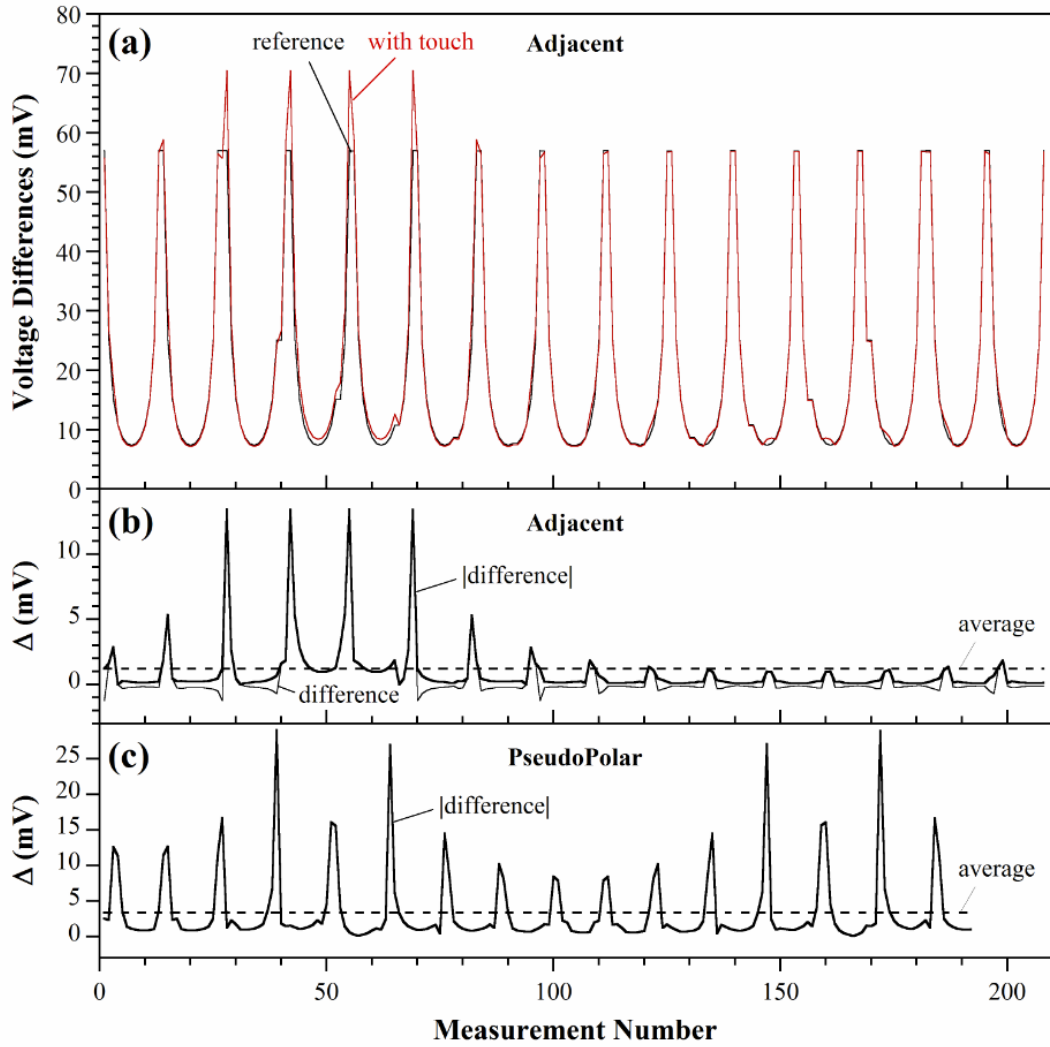


**Figure 2.2.** a) Boundary potentials  $\vec{V}_{touch}$  and  $\vec{V}_{ref}$  resulting from ADJ with (red) and without (black) a touch near the perimeter ( $x = 0.7$ ), respectively. b) The signal  $\Delta = \vec{V}_{touch} - \vec{V}_{ref}$  (thin line), the absolute value of  $\Delta$  (thick line), and the average of the signal  $\Delta$  (dashed line). c) For PP,  $|\Delta|$  and the mean of  $|\Delta|$ . Note the change in scale.

### 2.1.2 Performance Metrics

To evaluate the images resulting from the various injection patterns, the following metrics were employed (see Figure 2.3) based on definitions by others [24]. The performance metrics are illustrated in Figure 3.

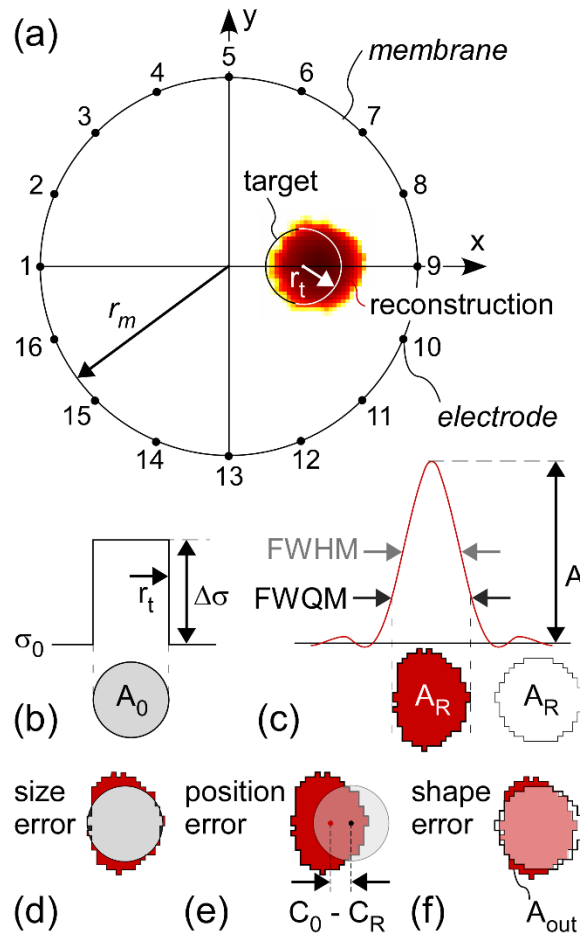


**Figure 2.3.** The metrics used to evaluate the reconstructions. a) A circular membrane with 16 electrodes at the boundary illustrating an original target stimulus at  $x = 0.5$  with radius  $r_t = 0.2$ , area  $A_0$ , and b) constant amplitude  $\Delta\sigma$  and c) the reconstructed image of a target with amplitude  $A$  and area  $A_R$ , defined as the region having values greater than the FWQM. The d) size, c) position, and e) shape errors.

The amplitude  $A$  of the reconstructed feature was defined as the maximum value in the image, obtained by averaging the 5 pixels with the largest values.

$$(4) \quad \text{Amplitude} = \text{Max}(\Delta\sigma)|_{\text{image}}$$

The reconstructed feature size  $A_R$  was taken as the area with pixels in the image having an amplitude greater than or equal to  $A/4$ , or the full width at quarter maximum (FWQM) in analogy with the standard full width at half max (FWHM). Using FWQM, the area of the target and the reconstruction were approximately equal for the smallest hyperparameter that could be used. Size error was then taken as the normalized difference between the reconstructed target area  $A_R$  and the original target area  $A_0$ . Positive size error indicates that the size of reconstructed target is greater than the size of the original target.

$$(5) \quad \text{Size Error} = (A_0 - A_R)/A_0$$

For positions  $x > 0.8$ , the size of the original target within the sensing area was reduced, which was taken into account.

Position error was defined as the distance between the center of the original target  $C_0$  and the weighted center of reconstructed target  $C_R$  (Figure 2.3d). A negative position error indicates that the center of the reconstructed target is closer to the center of the sensing membrane than the stimulus.

$$(6) \quad \text{Position Error} = C_0 - C_R$$

Shape error refers to the extent of distortion of the reconstructed stimulus from the circular one of the target. It was found by creating a circle of the same area,  $A_R$ , of radius  $r_R$  (Figure 2.3(c)) around the position  $C_R$  and then finding the area of the

reconstructed feature lying outside of that (Figure 2.3(e)), normalized by the area of the feature.

$$(7) \quad \text{Shape error} = A_{\text{OUT}} / A_{\text{R}}$$

For positions  $x > 0.8$ , the shape of the original target within the sensing area was no longer circular, so this metric was not used for those positions.

Signal to noise (SNR) was defined as the ratio of signal (mean of the  $|\Delta|$ ) and the standard deviation of the noise.

$$(8) \quad \text{SNR (in dB)} = 20 \log \left( \frac{E(|\Delta_i|)}{\sqrt{\text{Var}(\text{noise})}} \right)$$

## 2.2 Methods

EIDORS (version 3.9.1, MATLAB version R2018b) was used to solve both the forward and inverse problems. In simulations, a 2D sensing membrane with a normalized radius  $r_m = 1$  experienced a stimulus of radius  $r_t = 0.2 r_m$ . The target radius was chosen 0.2 because below this value the reconstructed target size did not change much. Around the periphery were 16 equally spaced point electrodes. Meshes were generated using the Netgen mesh generator, which were the same for all the injection patterns, depending only on the stimulus position.

The baseline conductivity of the membrane was fixed at  $\sigma_0 = 0.01 \text{ S/m} = 10 \text{ mS/m}$  and of the target  $\sigma_t = 0.6 \sigma_0$ , giving  $\Delta\sigma = 4 \text{ mS/m}$ . (Using a smaller conductivity change of  $\Delta\sigma = 0.4 \text{ mS/m}$  gave essentially the same results.) A current of 3 mA was injected into

one electrode and one electrode was made ground, based on the injection pattern. Voltage measurements (difference) were obtained making the measurements that involved the driving electrodes equal to zero.

Voltage measurements obtained from the forward problem  $\vec{V}_{touch}$  and  $\vec{V}_{ref}$  were used to solve the inverse problem. A baseline conductivity  $\sigma_0 = 0.01$  S/m was added as prior information. The hyperparameter ( $\lambda$ ) for noise free case was chosen to be the smallest one below which the reconstruction fails (i.e.  $\lambda = 4 \times 10^{-8}$ ). When noise was added, the hyperparameter was chosen based on the number of artifacts.

## 2.3 Results and Discussion

### 2.3.1 Comparison of Injection Patterns in Noise-Free Simulations

This section compares the performance of the three current injection patterns Figure 2.1(a) under the best possible conditions: noise free simulation data and using the smallest possible hyperparameter,  $\lambda = 4 \times 10^{-8}$ . The use of a nonzero  $\lambda$  is required to achieve a reconstruction; without it, the Jacobian matrix is too ill conditioned to be inverted.

Figure 2.4 shows the reconstructed images with a target conductivity change of -40% ( $\sigma_0 = 10$  mS/m,  $\Delta\sigma = -4$  mS/m), corresponding to an increase in resistance, at different positions between  $x = 0$  and 0.9. The adjacent (1,2) and pseudo-polar (1,8) patterns produced essentially identical images, despite the differences in the equipotential lines

and the voltage between injecting electrodes. The images resulting from polar injection (1,9) were, however, quite different. As shown in Figure 2.4c, at  $x = 0$  the area of the reconstructed target was larger—while its amplitude was smaller. At  $x = 0.1$ , the reconstructed target was distorted, being narrower in the  $x$ -direction, and it had a negative (blue) mirror image. The mirror moved symmetrically leftward as the target moved rightward, and it decreased in size. The presence of the mirror is known [25] and is a result of the symmetry of the injection pattern. The amplitude of the target increased at the edge of the sensing area.

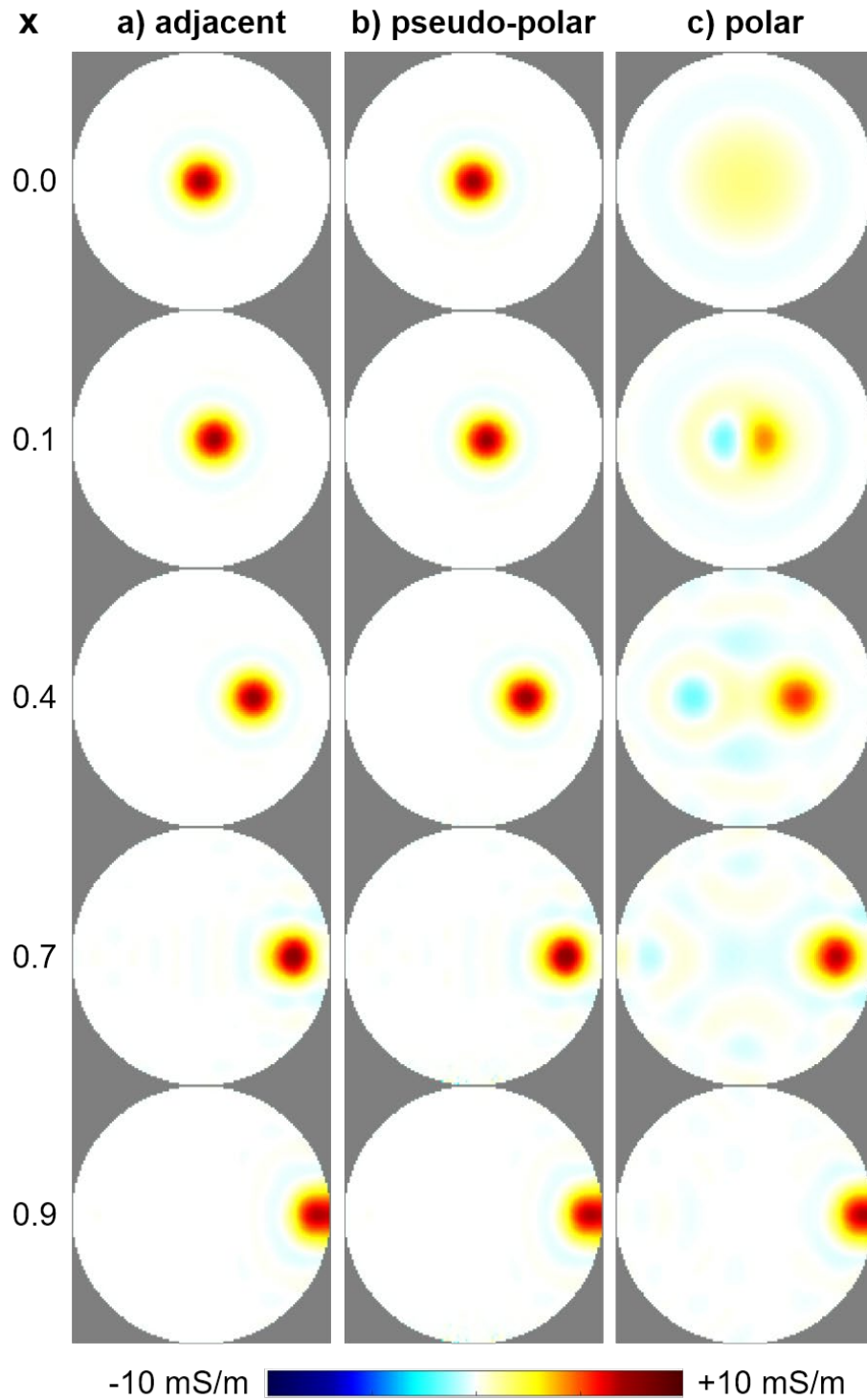


**Figure 2.4** EIT images reconstructed from noise free simulation data of targets positioned at various positions along the  $x$ -axis for a) adjacent b) pseudo-polar c) polar current injection patterns. The color indicates the amplitude of the reconstructed  $\Delta\sigma$  at each position. ( $\lambda = 4 \times 10^{-8}$ ,  $\sigma_0 = 0.01$  S/m,  $\Delta\sigma = 4$  mS/m).

To better compare the reconstructions, cross-sections across the center of the images ( $y = 0$ ) are shown in Figure 2.5. Heavy black lines indicate the two positions of the target at the center and near the edge; the dotted gray lines indicate positions where the target is so close to the edge that it touches it or extends partially outside the sensing area.

Although the stimulus was a cylinder with a constant amplitude of  $-4$  mS/m, the peaks in the reconstructed images were smooth, narrower curves with an amplitude of  $7$  S/m. For the adjacent and pseudo-polar injection patterns, as well as all of the other intermediate injection patterns (e.g. 1,3 to 1,7) the amplitude and width did not significantly change with the target position. (For a stimulus of  $-0.4$  mS/m, the peak at  $x = 0.7$  was not somewhat larger.) For the polar injection pattern, however, Figure 2.5(c) shows that the amplitude and width did depend on target position. In addition, the peak positions were incorrect, most notably when the target is at  $x = 0.1$  but even as far out as  $x = 0.6$ .

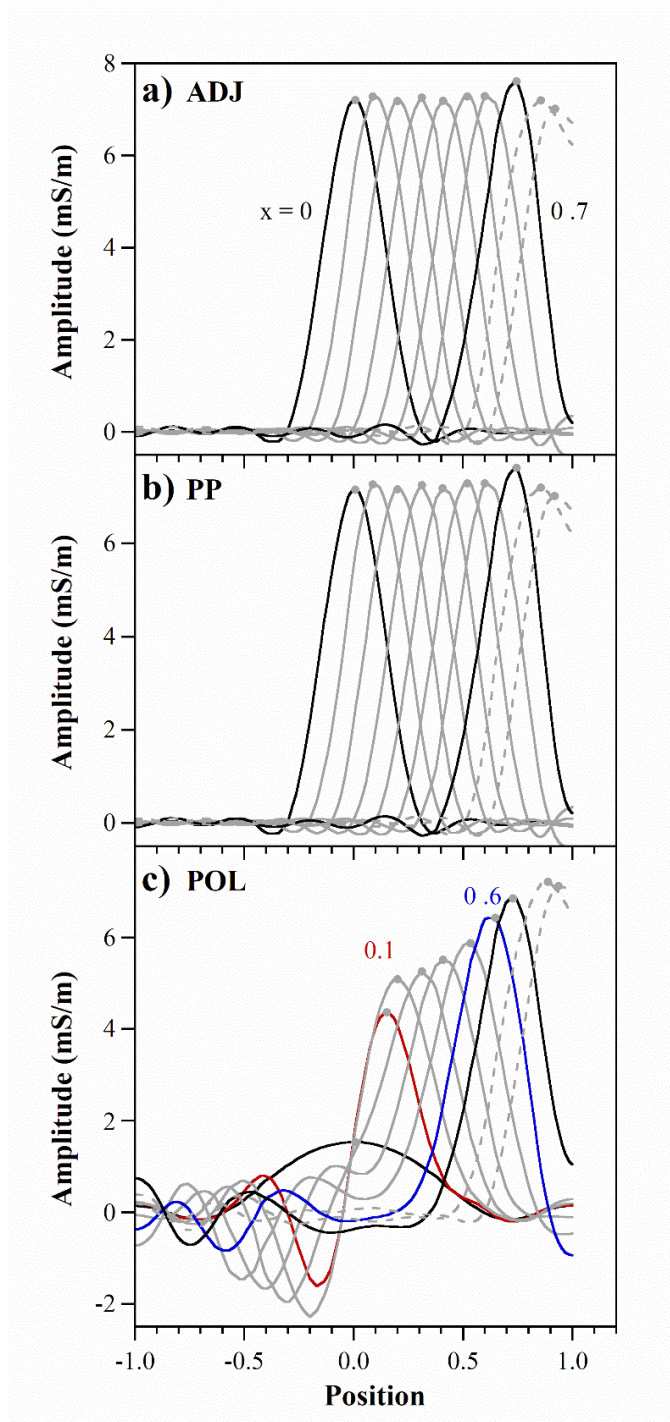


**Figure 2.5** Cross-sections taken along the  $x$ -axis of the reconstructed EIT images of Figure 2.4 showing amplitude as a function of the target position for a) adjacent b) pseudo-polar c) polar current injection patterns. Black lines indicate positions  $x = 0$  and  $0.7$ , gray lines show intermediate positions, and dashed lines show  $x = 0.8$  and  $0.9$ . Points indicate the maximum values.

The performance parameters (metrics) defined in Section 2.1.2 are shown for the three injection patterns in Figure 2.6. The size error (Figure 2.6(a)) was small (due to the choice of FWQM to define the feature area) and essentially constant with  $x$  for the adjacent and pseudo-polar patterns, increasing a little as the target approached the boundary at  $x = 0.8$ . Quantifying the size error for the polar pattern, it was maximum at  $x = 0$ , with the feature having over 5 times the original target area, giving an error of 450%. Just off center, at  $x = 0.1$ , when the highest symmetry was broken, the feature was substantially narrower. Above  $x = 0.3$  the size error for the POL pattern decreased with  $x$ , until it was equaled that of the other patterns at  $x = 0.8$ .

The position error (Figure 2.6(b)) was near zero for adjacent and pseudo-polar injection patterns, except, as expected, at  $x = 0.9$ , where it was positive, indicating that the weighted center was closer to the edge than the target was. For the polar pattern the position error was almost zero when the target was in the center, but it was large and negative (closer to the center) at  $x = 0.1$ . This error is related to the presence of the negative mirror image of the peak. The position error changed sign at larger  $x$ .

The shape error for the adjacent and pseudo-polar patterns was small. This error always has a positive value; the metric does not distinguish the direction of the distortion. At the edge ( $x = 0.8$ ) the shape error increased as the reconstructed peak became elongated (stretched) in the  $x$ -direction. For the polar pattern, as for the position error, the shape error was maximum at  $x = 0.1$  because of the distortion created by the negative mirror. The shape error then dropped until  $x = 0.7$ , after which it followed the trajectory of the adjacent and pseudo-polar patterns.

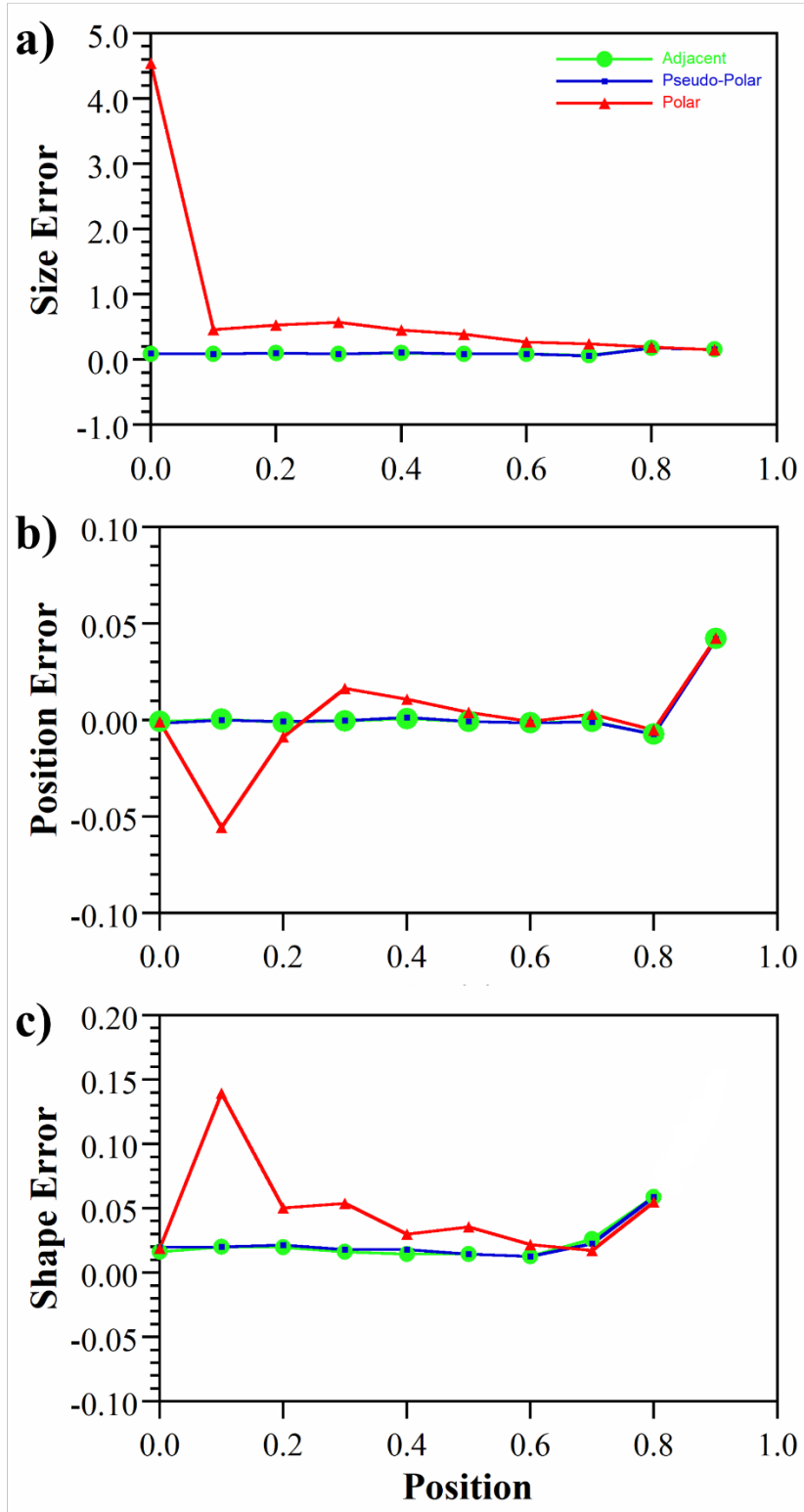


**Figure 2.6** Performance metrics for the three current injection patterns for the noise-free case ( $\lambda = 4 \times 10^{-8}$ ,  $\sigma_0 = 0.01$  S/m,  $\Delta\sigma = 4$  mS/m): a) size error, b) position error, and c) shape error vs  $x$ -position.

Under these ideal conditions, the choice of current injection pattern had no effect on the reconstructions, with the exception of the polar pattern. This might be considered somewhat surprising, given that the sensitivity of the adjacent pattern is lower in the center of the membrane than that of the pseudo-polar and polar patterns [26], but in all these cases the reconstructions were successful and artifact-free due to the lack of noise. Based on these results, it can be concluded that the polar pattern gives significant errors and no advantages, so it should not be used.

### 2.3.2 Comparison of Injection Patterns with Noise

Real data is not noise-free, so this section compares the different injection patterns when noise is added to the signal. Zero-centered white noise with standard deviation of  $3 \times 10^{-4}$  V was added to the boundary voltage vectors  $\vec{V}_{touch}$  and  $\vec{V}_{ref}$  from the forward problem to see the effect of noise on the reconstructed EIT image. Because the variances of independent random variables sum, the noise in their difference  $\Delta$  was  $\sqrt{2}\sigma_n$  larger. The target was placed at  $x = 0$  and was the same size as in the previous section ( $r_t = 0.2 r_m$ ,  $\sigma_0 = 10$  mS/m,  $\Delta\sigma = -4$  mS/m).

Using the same hyperparameter as for the noise-free data in Section 2.3.1 resulted in failed reconstructions, meaning that either no image resulted or that it was blank (see supporting information). Increasing the hyperparameter resulted in images, but they had artifacts. This occurs because the algorithm treats the high-spatial-frequency noise

as information. To avoid such “over-fitting” the hyperparameter had to be increased further. The hyperparameter now served a low-pass filtering role, resulting in smoothing. There has been extensive research on choosing optimal hyperparameter values to obtain the the most appropriate reconstructions [4, 27].

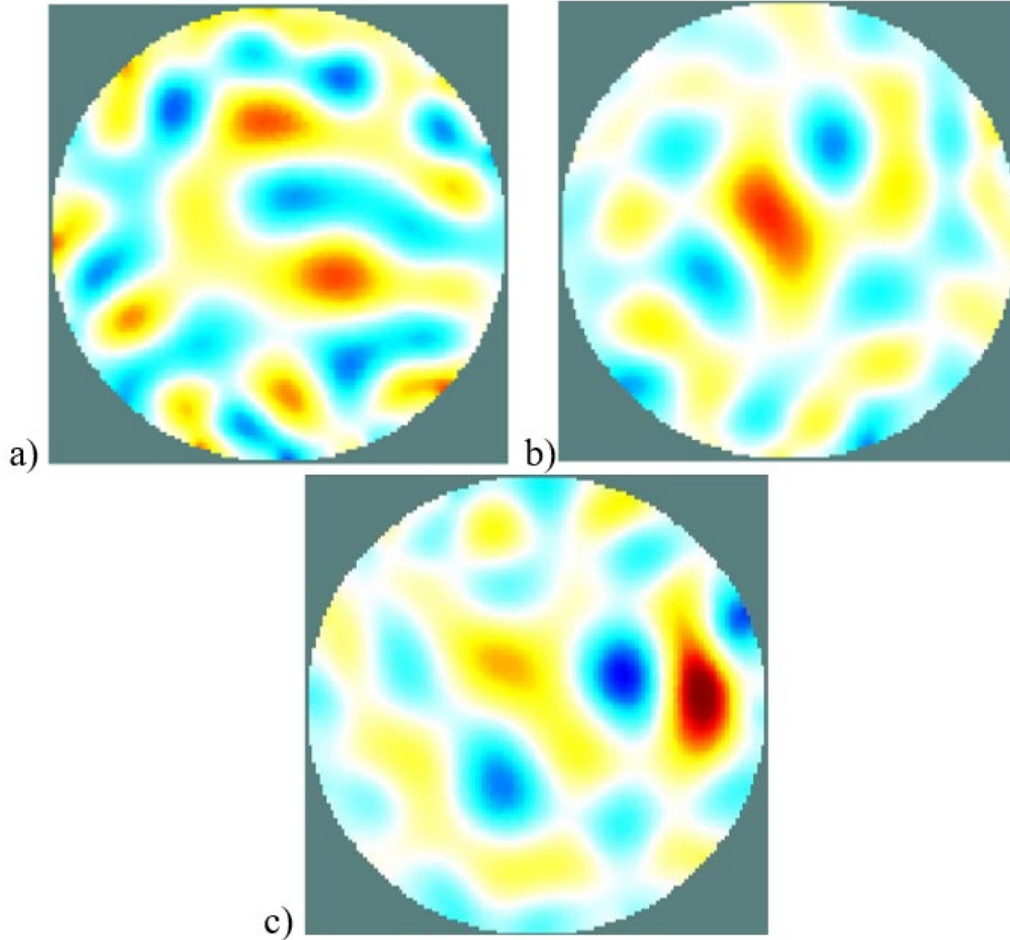


**Figure 2.7. Reconstructed images for a target at  $x = 0$  with  $3 \times 10^{-4}$  V of noise with a hyperparameter of  $\lambda = 2 \times 10^{-2}$  for a) adjacent (SNR = 3 dB) and b) pseudo polar (SNR = 12 dB) injections. c) For the same hyperparameter, the reconstruction for the adjacent pattern for a target at  $x = 0.7$  (SNR = 10 dB).**

Simulations were done 5 times for each pattern. Figure 2.7 shows one of the reconstructed images (see supporting information for other) using  $\lambda = 2 \times 10^{-2}$  for the adjacent and pseudo-polar injection patterns. The adjacent pattern (Figure 2.7a)

showed only artifacts at this  $\lambda$  for a target at center. The images varied significantly (as shown in the Supporting Information), but in no case did the target reconstruct. The pseudo-polar pattern (Figure 2.7(b)), while noisy, correctly placed a single target at the center, although it had obvious position and shape errors. The pseudo-polar injection pattern has an SNR 4 times the adjacent injection pattern. This result illustrates the key advantage of the higher SNR of the pseudo-polar pattern: successful reconstruction at a smaller  $\lambda$ . (It should be noted that even at this hyperparameter, in some cases the target was not identified or there were artifacts.) Figure 2.7(c) shows that for a target at  $x = 0.7$ , the adjacent pattern also resulted in generally successful reconstructions with few artifacts because of the larger signal size near the edge [28].

Note that for a sensing membrane, if the noise is independent of the current, then the SNR for the adjacent configuration can be raised simply by increasing the current or by lowering the membrane conductivity (increasing its resistance), both of which increase the voltage across the sensing electrodes. However, this results in greater power consumption by the sensor, and in addition larger currents will in general result in greater noise.

### **2.3.3 Effect of a Larger Hyperparameter**

As seen in the previous section, a larger hyperparameter is required when there is noise in the data. In this section the injection patterns are compared when a larger hyperparameter is used, without noise, so that the effect of the hyperparameter on the performance can be isolated.

Figure 2.8 shows reconstructed images for a hyperparameter that was 6 orders of magnitude larger than used in Section 2.3.1,  $\lambda = 2 \times 10^{-2}$ . Just as for  $\lambda = 4 \times 10^{-8}$ , there was no noticeable difference between the reconstructed images from the adjacent and pseudo-polar injection patterns. However, unlike in Section 2.3.1, the reconstructed target depended on its position. In addition, the images from the polar pattern look similar to the other patterns.

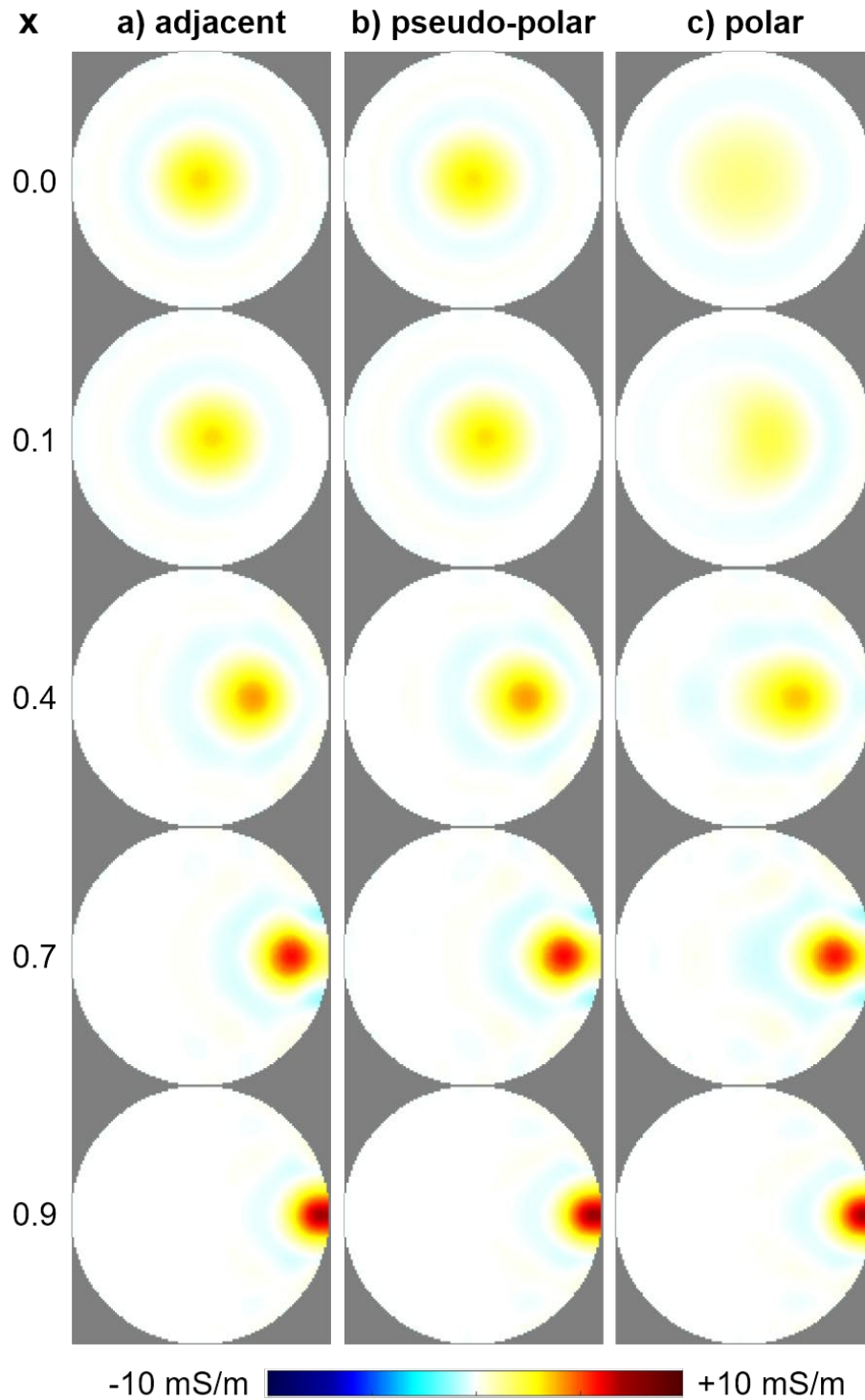


**Figure 2.8** EIT images reconstructed from noise-free simulation data with a larger hyperparameter,  $\lambda = 2 \times 10^{-2}$ , for the target at different positions for a) adjacent, b) pseudo-polar, and c) polar current injection patterns. ( $\sigma = 0.01$  S/m,  $\Delta\sigma = 4$  mS/m).

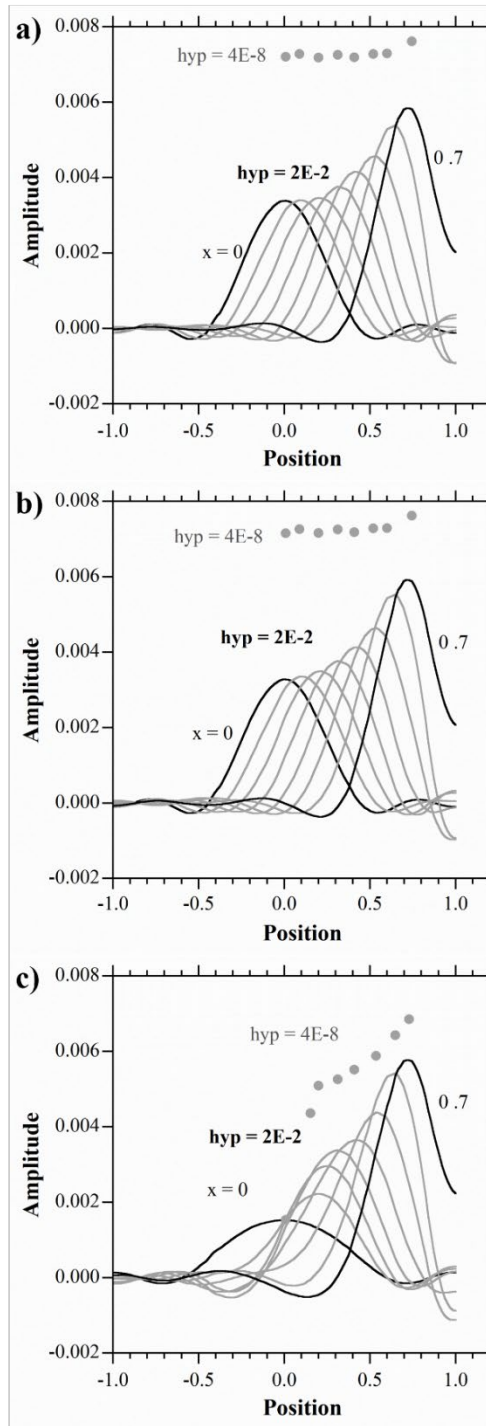


**Figure 2.9** Cross-sections along the x-axis of the reconstructed EIT images in Figure 2.8 showing amplitude as function of the target position for a) adjacent b) pseudo-polar c) polar current injection pattern.

The larger hyperparameter results in a dependence of the peak amplitude and area on the position of the target, with the amplitude falling in the center and the peak enlarging

in area. As was the case for the small hyperparameter, there was no noticeable difference between the reconstructed images from the adjacent and pseudo-polar patterns. Notably, the polar pattern produced images that were similar to the other two.

The corresponding cross-sections are shown in Figure 2.9 (the points indicate the amplitudes and peak positions for  $\lambda = 4 \times 10^{-8}$ ). The amplitude for the adjacent pattern is reduced by almost a factor of 2 at the center, and its width correspondingly increased. Even at the edge, the amplitude is reduced. The curves for the adjacent and pseudo-polar patterns are again essentially identical. The polar cross-sections resemble those of Figure 2.5, except that they are shorter and no longer have negative mirror images. The dependence of amplitude on position (see the Supporting Information for further discussion) means that amplitude cannot be used to obtain quantitative information about the strains induced by varying touch strengths. The size error also provides misleading visual information about the size of the touching object.

In general, smoothing does not reduce the volume under the curve. Thus, the volume under the curve was calculated by summing all the pixels whose values were greater than the FWQM. The volumes are shown as a function of position in Figure 2.10 for both values of  $\lambda$ . These values were almost constant, even for the polar pattern. Thus, for quantitative information about the deformation induced by a touch, the volume should be used.

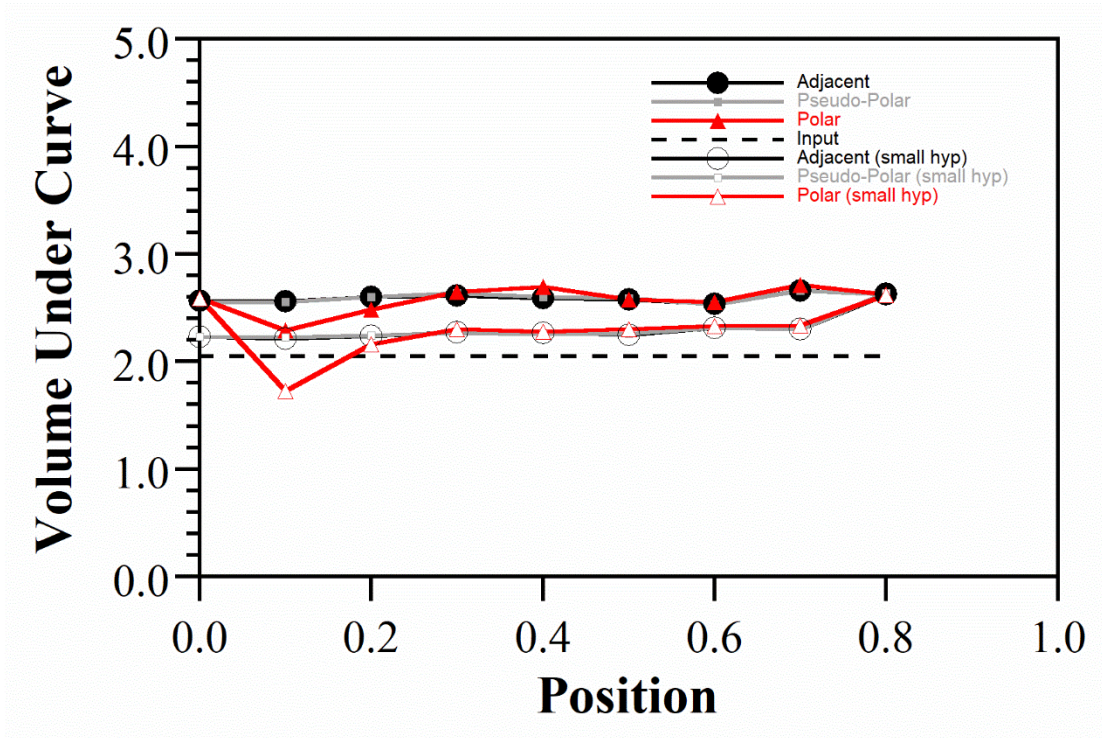


**Figure 2.10** The volume of the reconstructed feature, obtained by summing all pixels with values greater than FWQM. The horizontal dashed line shows the volume of the target.

The metrics for the injection patterns using  $\lambda = 2 \times 10^{-2}$  are shown in Figure 2.11. The size error increased significantly at the center for the adjacent and pseudo-polar patterns (compare Figure 2.6), and it remained large for the polar pattern. The position errors remained essentially unchanged when using the larger  $\lambda$ . Likewise, the shape errors remained near 2% for the adjacent and pseudo-polar patterns, increasing at the edge. For the polar pattern, the shape error at  $x = 0.1$  actually decreased because of the loss of the negative mirror image.

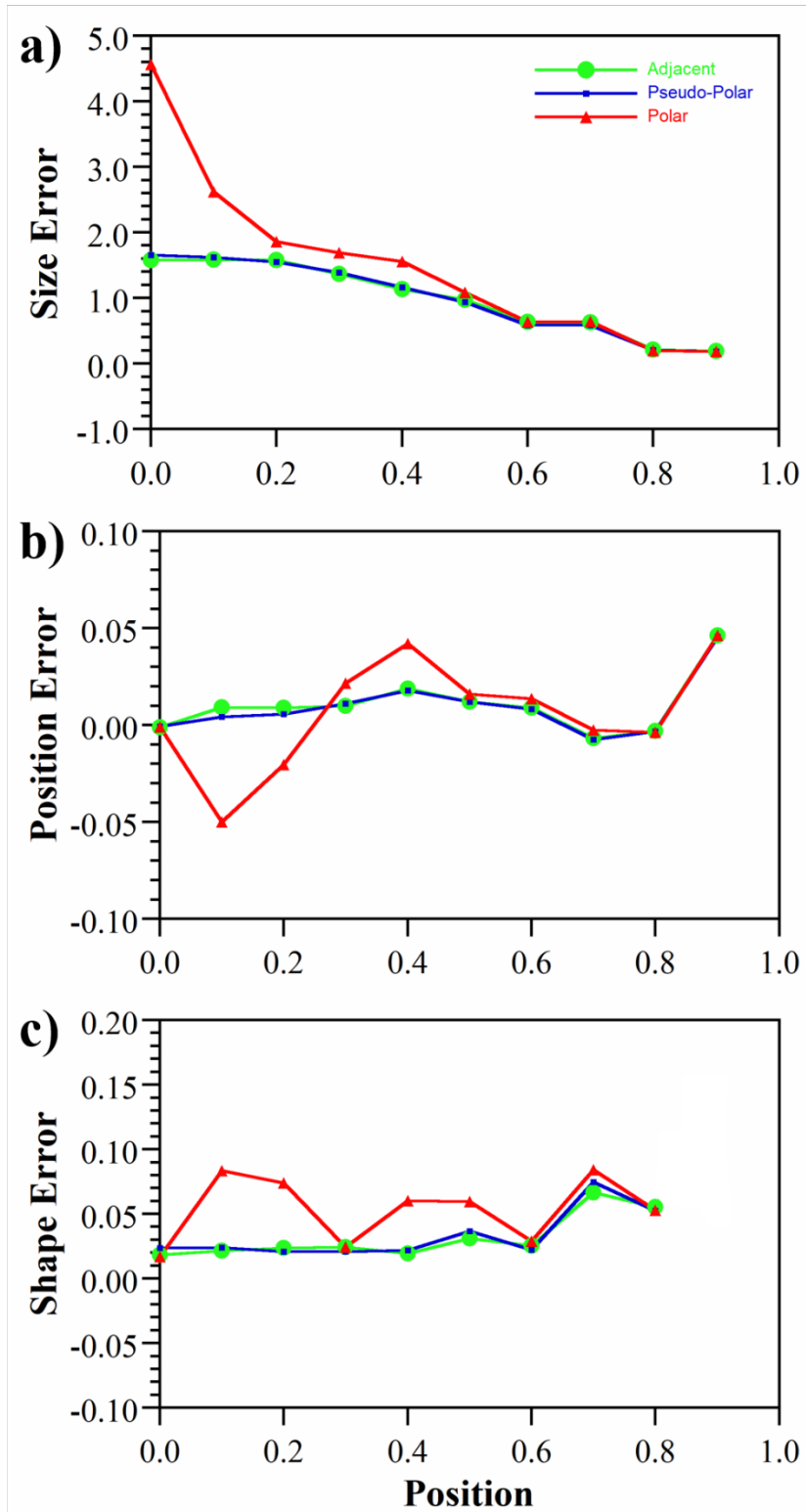


Figure 2.11 Performance metrics for the three current injection patterns for the noise-free case with  $\lambda = 2 \times 10^{-2}$  ( $\sigma_0 = 0.01$  S/m,  $\Delta\sigma = 4$  mS/m): a) size error, b) position error, and c) shape error.

## 2.4 Conclusions

The performance of commonly used injection patterns has been quantitatively compared for tactile sensing for the first time. All two-electrode injection patterns, except the polar pattern, when used with adjacent voltage measurement, a single round target of uniform  $\Delta\sigma$  on a uniform background  $\sigma_0$ , and the one-step Gauss-Newton method, produce identical reconstructions for the same hyperparameter. For the same constant current, tactile sensing benefits from using the pseudo-polar configuration because it has the largest SNR: the electrodes are further apart and thus have greater voltage differences. The larger SNR means that a smaller hyperparameter can be used, resulting in less smoothing. Because of its symmetry, the polar pattern gives poor results. To overcome the dependence of the reconstructed peak amplitude on target position when a large hyperparameter is needed, the volume under the peak can be used to determine the strength of a touch, since this volume remains independent of position and of hyperparameter.

### **Chapter 3. Concluding Remarks and Future Work**

In this thesis the effect of different current injection patterns on the reconstructed EIT image was studied using a target stimulus whose size and conductivity were fixed. This study for the first proves that, in the absence of the noise, any injection pattern can be used except polar for tactile sensing application, as there is no difference in the quantitative results. The results also show that for a system having noise, pseudo-polar injection pattern turns out to be the best having an SNR 4 times the adjacent injection pattern.

In future, further analysis can be performed to understand the quantitative performance of the tactile sensors by studying the effects of various parameters like background conductivity, target size, and conductivity on the reconstruction using EIDORS. In a sensor, involving multiple touches with different intensities would change the whole problem compared to a single touch; the effect of multiple touches on the reconstructed image and other performance metrics can be studied. This type of study can predict the ability of tactile sensors to distinguish between a big target and multiple small targets. Effect of different target shapes can also be studied. Also, in this study only one algorithm is used; in future a cross-validation study can be done using different types of algorithms.

In this study the touch input defined on the sensor is a cylindrical/step input which is not true for an actual piezoresistive sensor. In an actual sensor, strain profile of input touch has curvature. To simulate a real sensor there is need to apply multi-physics to the forward problem. Such a problem cannot be solved using EIDORS, so other FEM software like ANSYS, COMSOL can be used. For example, using a hyperelastic

material like rubber for modelling an actual tactile sensor and solving the forward problem using mechanical and electrical analysis. Using multi-physical simulations working of the 'Smart-Bra' can be simulated, which uses these sensors for detection of early breast cancer; which using the change in resistance can determine the difference between stiffness of a normal breast tissue and a cancerous lump.

## Appendix A. MATLAB Code

This MATLAB code was used to simulate the forward and inverse problem for a 2D tactile sensing medium, to obtain the reconstructed EIT image, and to obtain performance metrics. This derived from EIDORS tutorials. The author contributed some parts. This code should be used with EIDORS. EIDORS is open source software can be downloaded from: <http://eidors3d.sourceforge.net/>

```
%% FORWARD-INVERSE MODEL TO SOLVE FOR VOLTAGES AND
RECONSTRUCTED IMAGE (NORMAL SENSOR)

% EIDORS VERSION USED 3.9.1

% AYUSH NANKANI-UNIVERSITY OF MARYLAND, COLLEGE PARK

clear

close all

%% FORWARD PROBLEM

% DEFINING VARIABLES

ELEC_NUM = 16;% NUMBER OF ELECTRODES

CURRENT = 0.003;% CURRENT SUPPLIED IN AMPS

IMAGE_2D = 1;% IS IT A 2D IMAGE

for i=1:10 % DIFFERENT POSITION

INJ_PATT = [0,1];% [0,1] FOR ADJACENT [0,ELEC_NUM/2] FOR OPPOSITE
[0,(ELEC_NUM/2)-1] FOR NEARLY-OPPOSITE

MEAS_PATT = [0,1];% [0,1] FOR ADJACENT [0,ELEC_NUM/2] FOR
OPPOSITE [0,(ELEC_NUM/2)-1] FOR NEARLY-OPPOSITE
```

```

MODEL_TYPE = 'j2d4c';% FOR OTHER MODEL TYPES REFER TO
'mk_common_model'

OPTIONS = {'no_rotate_meas'...% OPEN 'mk_stim_patterns' FOR MORE OPTIONS
, 'no_meas_current'};

HYP = 2e-2;% HYPERPARAMETER VALUE

% SENSOR PROPERTIES

TARGET_SIZE = 0.2;% SIZE OF THE TARGET/ANOMALY

TARGET_POS = linspace(0,0.9,10);% POSITION OF THE TARGET/ANOMALY
[x,0]

MEM_CON = 0.01;% CONDUCTIVITY OF MEMBRANE

TARGET_CON = 0.6*MEM_CON;% CONDUCTIVITY OF TARGET/ANOMALY

% MODELLING THE SENSOR

calc_colours('clim',MEM_CON);

SENSOR_MODEL = mk_common_model(MODEL_TYPE, ELEC_NUM);%

MODEL THE SENSOR

IMG1 = mk_image(SENSOR_MODEL, MEM_CON);% INITIAL IMAGE OF THE
SENSOR

IMG_FEM = figure;

F1 = subplot(121);% PLOTTING FEM OF INITIAL IMAGE

show_fem(IMG1);% FEM OF INITIAL IMAGE

IMG2 = IMG1;

```

```

TARGET = sprintf('(x-%f).^2+(y).^2<%f^2',TARGET_POS(i),TARGET_SIZE);

ADD_LAYER1 = inline(TARGET,'x','y','z');% ADDING ANOTHER
LAYER/TARGET

IMG2.elem_data = IMG2.elem_data - ((MEM_CON-TARGET_CON)*...
elem_select(IMG2.fwd_model, ADD_LAYER1));% CHANGING THE
CONDUCTIVITY OF THE ADDITIONAL LAYER

F2 = subplot(122);% PLOTTING FEM OF INITIAL IMAGE

show_fem(IMG2);% FEM OF FINAL IMAGE

% SOLVING FORWARD PROBLEM (FOR VOLTAGES)

[stim, meas_sel] = mk_stim_patterns(ELEC_NUM,IMAGE_2D,INJ_PATT,...
MEAS_PATT,OPTIONS,CURRENT);% CALCULATE THE STIMULATION
PATTERN

IMG1.fwd_model.stimulation = stim;

IMG1.fwd_solve.get_elec_curr = 1;

IMG1.fwd_solve.get_all_meas = 1;

BASE_VOLT = fwd_solve(IMG1);% VOLTAGES FOR INITIAL/BASE IMAGE

IMG2.fwd_model.stimulation = stim;

IMG2.fwd_solve.get_elec_curr = 1;

IMG2.fwd_solve.get_all_meas = 1;

CURR_VOLT = fwd_solve(IMG2);% VOLTAGES FOR FINAL/CURRENT
IMAGE

```

```

%% VIEW VOLTAGE PATTERN

% OPTIONS1 = [0,1];

% IMG_VOLT = figure;

% %F3 = subplot(121);

% VIEW = rmfield(IMG2, 'elem_data');

% VIEW.node_data = BASE_VOLT.volt(:,12);% WITHOUT TARGET
(HOMOGENOUS)

% V = show_fem(VIEW,OPTIONS1); axis off% WITH TARGET
(INHOMOGENOUS)

% % F4 = subplot(122);

% % VIEW = rmfield(IMG2, 'elem_data');

% % VIEW.node_data = CURR_VOLT.volt(:,1);

% % show_fem(VIEW,OPTIONS1); axis equal

% % VIEW.node_data = BASE_VOLT.volt(:,1) - CURR_VOLT.volt(:,1);%
DIFFERENCE IMAGE

% % F5 = subplot(133);

% % show_fem(VIEW); axis equal

% % IMG2.calc_colours.cb_shrink_move = [0.4,.5,-0.05];

% % common_colourbar([F3,F4],IMG2);

%% VIEW CURRENT PATTERN

% IMG1.fwd_model.mdl_slice_mapper.npx = 64;

% IMG1.fwd_model.mdl_slice_mapper.npy = 64;

```

```

% IMG_CURRENT = figure;

% show_current(IMG1,BASE_VOLT.volt(:,1));

% %CUR_VAL = CUR_MAP.xc(32,32)

% INVERSE PROBLEM

% VOLTAGE DATA (CONVERTING THE DATA FROM FORWARD PROBLEM
INTO PROPER FORM FOR INVERSE PROBLEM)

BASE_IMAGE_LN = BASE_VOLT.meas + (3E-
5*randn(size(BASE_VOLT.meas)));% ADDING LOW NOISE TO BASE IMAGE

BASE_IMAGE_MN = BASE_VOLT.meas + (1E-
4*randn(size(BASE_VOLT.meas)));% ADDING MEDIUM NOISE TO BASE
IMAGE

BASE_IMAGE_HN = BASE_VOLT.meas + (3E-
4*randn(size(BASE_VOLT.meas)));% ADDING HIGH NOISE TO BASE IMAGE

CUR_IMAGE_LN = CURR_VOLT.meas + (3E-
5*randn(size(CURR_VOLT.meas)));% ADDING LOW NOISE TO CURRENT
IMAGE

CUR_IMAGE_MN = CURR_VOLT.meas + (1E-
4*randn(size(CURR_VOLT.meas)));% ADDING MEDIUM NOISE TO CURRENT
IMAGE

CUR_IMAGE_HN = CURR_VOLT.meas + (3E-
4*randn(size(CURR_VOLT.meas)));% ADDING HIGH NOISE TO CURRENT
IMAGE

```

```

% SENSOR MODEL

SENSOR_MODEL = mk_common_model(MODEL_TYPE, ELEC_NUM);

SENSOR_MODEL.fwd_model.stimulation = stim;

SENSOR_MODEL.fwd_model.meas_select = meas_sel;

SENSOR_MODEL.solve = @nodal_solve;

% SENSOR_MODEL.solve = @inv_solve_diff_GN_one_step;

% SENSOR_MODEL.solve = @inv_solve_TV_pdipm;

% SENSOR_MODEL.R_prior = @prior_TV;

% SENSOR_MODEL.parameters.max_iterations = 10;

% SENSOR_MODEL.parameters.term_tolerance = 1e-3;

% SENSOR_MODEL.RtR_prior = @prior_tikhonov;

% SENSOR_MODEL.RtR_prior = @prior_noser;

SENSOR_MODEL.RtR_prior = @prior_laplace;

SENSOR_MODEL.hyperparameter.value = HYP;

SENSOR_MODEL.jacobian_bkgnd.value = MEM_CON;

% EIT IMAGE

MAX_DIFF(i) = max(CURR_VOLT.meas - BASE_VOLT.meas); % MAXIMUM
VOLTAGE DIFFERENCE

EIT_IMG = inv_solve(SENSOR_MODEL, CURR_VOLT.meas,
BASE_VOLT.meas); % SOLVING THE INVERSE PROBLEM

IMG_EIT = figure;

```

```

AMP(1,i) = max(abs(EIT_IMG.node_data))% IF USING NODAL SOLVER
% AMP(1,i) = max(abs(EIT_IMG.elem_data));% IF USING ELEMENT SOLVER
% MAX_READ = 0.001;
MAX_READ = max(abs(EIT_IMG.node_data));
% MAX_READ = max(abs(EIT_IMG.elem_data));
calc_colours('npoints',128);% PLOT THE IMAGE IN ABSOLUTE VALUES
calc_colours('clim',MAX_READ);
show_slices(EIT_IMG);% SHOW SLICES OF RECONSTRUCTED IMAGE
(ABSOLUTE VALUES)
eidors_colourbar(EIT_IMG);% PLOT THE COLOR BAR
title(sprintf('NORMAL MEMBRANE HYP = %0.2E Max. Value = %f',...
HYP, max(abs(EIT_IMG.node_data))));% PRINT THE TITLE
% title(sprintf('NORMAL MEMBRANE HYP = %0.2E Max. Value = %f',...
% HYP, max(abs(EIT_IMG.elem_data))));% PRINT THE TITLE (ELEMENT
SOLVER)
SAVE = sprintf('EIT IMG HYP=%g InjElec=%g
LP=%g.tif',HYP,INJ_PATT(1,2),TARGET_POS(i));
saveas(IMG_EIT,SAVE);
OUT_IMG = calc_slices(EIT_IMG, [Inf,Inf,0]);% SHOW SLICES OF
RECONSTRUCTED IMAGE
% IMG_EIT_SURF = figure;
% surf(flipud(OUT_IMG));% SURFACE PLOT (3D)
IMG_EIT_CRSEC = figure;

```

```

plot(OUT_IMG(64,2:127));

% EIT IMAGE (LOW NOISE)

MAX_DIFF_LN = max(CUR_IMAGE_LN-BASE_IMAGE_LN);% MAXIMUM
VOLTAGE DIFFERENCE

EIT_IMG_LN = inv_solve(SENSOR_MODEL, CUR_IMAGE_LN,
BASE_IMAGE_LN);% SOLVING THE INVERSE PROBLEM

IMG_EIT_LN = figure;

AMP_LN(1,i) = max(abs(EIT_IMG_LN.node_data));

% AMP_LN(1,i) = max(abs(EIT_IMG_LN.elem_data));

MAX_READ_LN = max(abs(EIT_IMG_LN.node_data));

% MAX_READ_LN = max(abs(EIT_IMG_LN.elem_data))

calc_colours('npoints',128);% PLOT THE IMAGE IN ABSOLUTE VALUES

calc_colours('clim',MAX_READ_LN);

show_slices(EIT_IMG_LN);% SHOW SLICES OF RECONSTRUCTED IMAGE
(ABSOLUTE VALUES)

eidors_colourbar(EIT_IMG_LN);% PLOT THE COLOR BAR

title(sprintf('NORMAL MEMBRANE HYP = %0.2E Max. Value = %f',...
HYP, max(abs(EIT_IMG_LN.node_data))));% PRINT THE TITLE

% title(sprintf('NORMAL MEMBRANE HYP = %0.2E Max. Value = %f',...
% HYP, max(abs(EIT_IMG_LN.elem_data))));% PRINT THE TITLE

OUT_IMG_LN = calc_slices(EIT_IMG_LN, [Inf,Inf,0]);% SHOW SLICES OF
RECONSTRUCTED IMAGE

```

```

% IMG_EIT_LN_SURF = figure;

% surf(flipud(OUT_IMG_LN));% SURFACE PLOT (3D)

% IMG_EIT_LN_CRSEC = figure;

% plot(OUT_IMG_LN(64,2:127));% PLOT THE CROSS-SECTION OF THE
IMAGE

% EIT IMAGE (MEDIUM NOISE)

MAX_DIFF_MN = max(CUR_IMAGE_MN-BASE_IMAGE_MN);% MAXIMUM
VOLTAGE DIFFERENCE

EIT_IMG_MN = inv_solve(SENSOR_MODEL, CUR_IMAGE_MN,
BASE_IMAGE_MN);% SOLVING THE INVERSE PROBLEM

IMG_EIT_MN = figure;

AMP_MN(1,i) = max(abs(EIT_IMG_MN.node_data));

%AMP_MN(1,i) = max(abs(EIT_IMG.elem_data));

MAX_READ_MN = max(abs(EIT_IMG_MN.node_data))

%MAX_READ_MN = max(abs(EIT_IMG_MN.elem_data))

calc_colours('npoints',128);% PLOT THE IMAGE IN ABSOLUTE VALUES

calc_colours('clim',MAX_READ_MN);

show_slices(EIT_IMG_MN);% SHOW SLICES OF RECONSTRUCTED IMAGE
(ABSOLUTE VALUES)

eidors_colourbar(EIT_IMG_MN);% PLOT THE COLOR BAR

title(sprintf('NORMAL MEMBRANE HYP = %0.2E Max. Value = %f',...
HYP, max(abs(EIT_IMG_MN.node_data))));

```

```

% title(sprintf('NORMAL MEMBRANE HYP = %0.2E Max. Value = %f,...
% HYP, max(abs(EIT_IMG_MN.elem_data))));% PRINT THE TITLE

OUT_IMG_MN = calc_slices(EIT_IMG_MN, [Inf,Inf,0]); % SHOW SLICES OF
RECONSTRUCTED IMAGE

% IMG_EIT_MN_SURF = figure;

% surf(flipud(OUT_IMG3));% SURFACE PLOT (3D)

% IMG_EIT_MN_CRSEC = figure;

% plot(OUT_IMG3(64,2:127));% PLOT THE CROSS-SECTION OF THE IMAGE

% EIT IMAGE (HIGH NOISE)

MAX_DIFF_HN = max(CUR_IMAGE_HN-BASE_IMAGE_HN);% MAXIMUM
VOLTAGE DIFFERENCE

EIT_IMG_HN = inv_solve(SENSOR_MODEL, CUR_IMAGE_HN,
BASE_IMAGE_HN); % SOLVING THE INVERSE PROBLEM

IMG_EIT_HN = figure;

AMP_HN(1,i) = max(abs(EIT_IMG_HN.node_data));

% AMP_HN(1,i) = max(abs(EIT_IMG.elem_data));

MAX_READ_HN = max(abs(EIT_IMG_HN.node_data));

% MAX_READ_HN = max(abs(EIT_IMG_HN.elem_data));

calc_colours('npoints',128);% PLOT THE IMAGE IN ABSOLUTE VALUES

calc_colours('clim',MAX_READ_HN);

show_slices(EIT_IMG_HN);% SHOW SLICES OF RECONSTRUCTED IMAGE
(ABSOLUTE VALUES)

```

```

eidors_colourbar(EIT_IMG_HN);% PLOT THE COLOR BAR

title(sprintf('NORMAL MEMBRANE HYP = %0.2E Max. Value = %f',...
HYP, max(abs(EIT_IMG_HN.node_data))));% PRINT THE TITLE

% title(sprintf('NORMAL MEMBRANE HYP = %0.2E Max. Value = %f',...
% HYP, max(abs(EIT_IMG_HN.node_data))));% PRINT THE TITLE

OUT_IMG_HN = calc_slices(EIT_IMG_HN, [Inf,Inf,0]);% SHOW SLICES OF
RECONSTRUCTED IMAGE

% IMG_EIT_HN_SURF = figure;

% surf(flipud(OUT_IMG4));% SURFACE PLOT (3D)

% IMG_EIT_HN_CRSEC = figure;

% plot(OUT_IMG4(64,2:127));% PLOT THE CROSS-SECTION OF THE IMAGE

%% POST PROCESSING

% FULL WIDTH HALF MAX

HMAX = (min(abs(EIT_IMG.node_data)) + max(abs(EIT_IMG.node_data)))*
0.25;% FIND HALFMAX

INDEX1 = find(EIT_IMG.node_data >= HMAX, 1, 'first');% FIND WHERE THE
DATA FIRST DROPS BELOW HALF THE MAX.

INDEX2 = find(EIT_IMG.node_data >= HMAX, 1, 'last');% FIND WHERE THE
DATA FIRST RISES ABOVE HALF THE MAX.

FWHM = INDEX2-INDEX1 + 1;% FWHM IN INDEXES.

FWHMX = EIT_IMG.node_data(INDEX2) - EIT_IMG.node_data(INDEX1);

NEW_IMG=EIT_IMG;

```

```

str=0;

I=size(EIT_IMG.node_data);

for N=1:I(1,1)

    if (NEW_IMG.node_data(N))<=HMAX

        NEW_IMG.node_data(N)=0;

    else

str=str+1;

    end

end

IMG_EIT_FWHM = figure;

% calc_colours('npoints',128);% PLOT THE IMAGE IN ABSOLUTE VALUES

% calc_colours('clim',MAX_READ);

show_slices(NEW_IMG);% SHOW SLICES OF RECONSTRUCTED IMAGE

(ABSOLUTE VALUES)

eidors_colourbar(NEW_IMG);% PLOT THE COLOR BAR

title(sprintf('HYP = %0.2E Max. Value = %f,...

HYP, max(abs(NEW_IMG.node_data))));% PRINT THE TITLE

SAVE = sprintf('FWHM HYP=%g InjElec=%g

LP=%g.tif,HYP,INJ_PATT(1,2),TARGET_POS(i));

saveas(IMG_EIT_FWHM,SAVE);

OUT_IMG_FWHM = calc_slices(NEW_IMG, [Inf,Inf,0]);% SHOW SLICES OF

RECONSTRUCTED IMAGE

% IMG_EIT_FWHM_SURF = figure;

```

```

% surf(flipud(OUT_IMG_FWHM));% SURFACE PLOT (3D)

% IMG_EIT_FWHM_CRSEC = figure;

% plot(OUT_IMG_FWHM(64,2:127));% PLOT THE CROSS-SECTION OF THE
IMAGE

% LOW NOISE

HMAX_LN = (min(EIT_IMG_LN.node_data) + max(EIT_IMG_LN.node_data))
*0.25;% FIND HALFMAX

INDEX1_LN = find(EIT_IMG_LN.node_data >= HMAX_LN, 1, 'first');% FIND
WHERE THE DATA FIRST DROPS BELOW HALF THE MAX.

INDEX2_LN = find(EIT_IMG_LN.node_data >= HMAX_LN, 1, 'last');% FIND
WHERE THE DATA FIRST RISES ABOVE HALF THE MAX.

FWHM_LN = INDEX2_LN-INDEX1_LN + 1;% FWHM IN INDEXES.

FWHMX_LN = EIT_IMG_LN.node_data(INDEX2_LN) - ...

EIT_IMG_LN.node_data(INDEX1_LN);

NEW_IMG_LN=EIT_IMG_LN;

str=0;

I3=size(EIT_IMG_LN.node_data);

for N=1:1:I3(1,1)

    if (NEW_IMG_LN.node_data(N))<=HMAX_LN

        NEW_IMG_LN.node_data(N)=0;

    else

str=str+1;

```

```

end

end

IMG_EIT_FWHM_LN = figure;

% calc_colours('npoints',128);% PLOT THE IMAGE IN ABSOLUTE VALUES

% calc_colours('clim',MAX_READ_MN);

show_slices(NEW_IMG_LN);% SHOW SLICES OF RECONSTRUCTED IMAGE

(ABSOLUTE VALUES)

eidors_colourbar(NEW_IMG_LN);% PLOT THE COLOR BAR

title(sprintf('HYP = %0.2E Max. Value = %f,...
HYP, max(abs(NEW_IMG_LN.node_data))));% PRINT THE TITLE

OUT_IMG_LN_FWHM = calc_slices(NEW_IMG_LN, [Inf,Inf,0]);% SHOW

SLICES OF RECONSTRUCTED IMAGE

% IMG_EIT_FWHM_LN_SURF = figure;

% surf(flipud(OUT_IMG_LN_FWHM));% SURFACE PLOT (3D)

% IMG_EIT_FWHM_LN_CRSEC = figure;

% plot(OUT_IMG_LN_FWHM(64,2:127));% PLOT THE CROSS-SECTION OF

THE IMAGE

% MEDIUM NOISE

HMAX_MN = (min(EIT_IMG_MN.node_data) + max(EIT_IMG_MN.node_data))

*0.25;% FIND HALFMAX

INDEX1_MN = find(EIT_IMG_MN.node_data >= HMAX_MN, 1, 'first');% FIND

WHERE THE DATA FIRST DROPS BELOW HALF THE MAX.

```

```

INDEX2_MN = find(EIT_IMG_MN.node_data >= HMAX_MN, 1, 'last');% FIND
WHERE THE DATA FIRST RISES ABOVE HALF THE MAX.

FWHM_MN = INDEX2_MN-INDEX1_MN + 1;% FWHM IN INDEXES.

FWHMX_MN = EIT_IMG_MN.node_data(INDEX2_MN) - ...
EIT_IMG_MN.node_data(INDEX1_MN);

NEW_IMG_MN=EIT_IMG_MN;

str=0;

I3=size(EIT_IMG_MN.node_data);

for N=1:1:I3(1,1)

    if (NEW_IMG_MN.node_data(N))<=HMAX_MN

        NEW_IMG_MN.node_data(N)=0;

    else

        str=str+1;

    end

end

IMG_EIT_FWHM_MN = figure;

% calc_colours('npoints',128);% PLOT THE IMAGE IN ABSOLUTE VALUES

% calc_colours('clim',MAX_READ_MN);

show_slices(NEW_IMG_MN);% SHOW SLICES OF RECONSTRUCTED IMAGE
(ABSOLUTE VALUES)

eidors_colourbar(NEW_IMG_MN,0);% PLOT THE COLOR BAR

title(sprintf('HYP = %0.2E Max. Value = %f',...
HYP, max(abs(NEW_IMG_MN.node_data))));% PRINT THE TITLE

```

```

OUT_IMG_MN_FWHM = calc_slices(NEW_IMG_MN, [Inf,Inf,0]);% SHOW
SLICES OF RECONSTRUCTED IMAGE

% IMG_EIT_FWHM_MN_SURF = figure;

% surf(flipud(OUT_IMG_MN_FWHM));% SURFACE PLOT (3D)

% IMG_EIT_FWHM_MN_CRSEC = figure;

% plot(OUT_IMG_MN_FWHM(64,2:127));% PLOT THE CROSS-SECTION OF
THE IMAGE

% HIGH NOISE

HMAX_HN = (min(EIT_IMG_HN.node_data) +
max(EIT_IMG_HN.node_data))*0.25;% FIND HALFMAX

INDEX1_HN = find(EIT_IMG_HN.node_data >= HMAX_HN, 1, 'first');% FIND
WHERE THE DATA FIRST DROPS BELOW HALF THE MAX.

INDEX2_HN = find(EIT_IMG_HN.node_data >= HMAX_HN, 1, 'last');% FIND
WHERE THE DATA FIRST RISES ABOVE HALF THE MAX.

FWHM_HN = INDEX2_HN-INDEX1_HN + 1;% FWHM IN INDEXES.

FWHMX_HN = EIT_IMG_HN.node_data(INDEX2_HN) - ...
EIT_IMG_HN.node_data(INDEX1_HN);% OR, if you have an x vector

NEW_IMG_HN=EIT_IMG_HN;

str=0;

I3=size(EIT_IMG_HN.node_data);

for N=1:I3(1,1)

    if (NEW_IMG_HN.node_data(N))<=HMAX_HN

```

```

    NEW_IMG_HN.node_data(N)=0;

else

str=str+1;

end

end

IMG_EIT_FWHM_HN = figure;

% calc_colours('npoints',128);% PLOT THE IMAGE IN ABSOLUTE VALUES

% calc_colours('clim',MAX_READ_HN);

show_slices(NEW_IMG_HN);% SHOW SLICES OF RECONSTRUCTED IMAGE

(ABSOLUTE VALUES)

eidors_colourbar(NEW_IMG_HN);% PLOT THE COLOR BAR

title(sprintf('HYP = %0.2E Max. Value = %f,...

HYP, max(abs(NEW_IMG_HN.node_data))));% PRINT THE TITLE

OUT_IMG_HN_FWHM = calc_slices(NEW_IMG_HN, [Inf,Inf,0]);% SHOW

SLICES OF RECONSTRUCTED IMAGE

% IMG_EIT_FWHM_HN_SURF = figure;

% surf(flipud(OUT_IMG_HN_FWHM));% SURFACE PLOT (3D)

% IMG_EIT_FWHM_HN_CRSEC = figure;

% plot(OUT_IMG_HN_FWHM(64,2:127));% PLOT THE CROSS-SECTION OF

THE IMAGE

CRSEC_DATA(:,i) = OUT_IMG(64,2:127);

figure(99);

```

```

CRSEC = plot(OUT_IMG(64,2:127));

hold on

CRSEC_FWHM_DATA(:,i) = OUT_IMG_FWHM(64,2:127);

figure(100);

CRSEC_FWHM = plot(OUT_IMG_FWHM(64,2:127));

hold on

CRSEC_LN_DATA(:,i) = OUT_IMG_LN(64,2:127);

figure(101);

CRSEC_LN = plot(OUT_IMG_LN(64,2:127));

hold on

CRSEC_LN_FWHM_DATA(:,i) = OUT_IMG_LN_FWHM(64,2:127);

figure(102);

CRSEC_LN_FWHM = plot(OUT_IMG_LN_FWHM(64,2:127));

hold on

CRSEC_MN_DATA(:,i) = OUT_IMG_MN(64,2:127);

figure(103);

CRSEC_MN = plot(OUT_IMG_MN(64,2:127));

hold on

CRSEC_MN_FWHM_DATA(:,i) = OUT_IMG_MN_FWHM(64,2:127);

figure(104);

CRSEC_MN_FWHM = plot(OUT_IMG_MN_FWHM(64,2:127));

hold on

CRSEC_HN_DATA(:,i) = OUT_IMG_HN(64,2:127);

```

```

figure(105);
CRSEC_HN = plot(OUT_IMG_HN(64,2:127));
hold on
CRSEC_HN_FWHM_DATA(:,i) = OUT_IMG_HN_FWHM(64,2:127);
figure(106);
CRSEC_HN_FWHM = plot(OUT_IMG_HN_FWHM(64,2:127));
hold on
c=0;
for a = 1:128
    for b = 1:128
        if isnan(OUT_IMG_FWHM(a,b))
            OUT_IMG_FWHM(a,b)=0;
        else
            c=c+1;
        end
    end
end
end

SUMOA(i)= sum(OUT_IMG_FWHM, 'all');

%% METRICS
PARAM = [TARGET_POS(i);0;0;TARGET_SIZE];
METRICS(:,i) = eval_GREIT_fig_merit(EIT_IMG, PARAM);
% METRICS_LN(:,i) = eval_GREIT_fig_merit(EIT_IMG_LN, PARAM);

```

```

% METRICS_MN(:,i) = eval_GREIT_fig_merit(EIT_IMG_MN, PARAM);
% METRICS_HN(:,i) = eval_GREIT_fig_merit(EIT_IMG_HN, PARAM);

SNR_LN(i) = 20*log10(mean(abs(CUR_IMAGE_LN-
BASE_IMAGE_LN))/std((CUR_IMAGE_LN-CURR_VOLT.meas)-
(BASE_IMAGE_LN-BASE_VOLT.meas)));

SNR_MN(i) = 20*log10(mean(abs(CUR_IMAGE_MN-
BASE_IMAGE_MN))/std((CUR_IMAGE_MN-CURR_VOLT.meas)-
(BASE_IMAGE_MN-BASE_VOLT.meas)));

SNR_HN(i) = 20*log10(mean(abs(CUR_IMAGE_HN-
BASE_IMAGE_HN))/std((CUR_IMAGE_HN-CURR_VOLT.meas)-
(BASE_IMAGE_HN-BASE_VOLT.meas)));

end

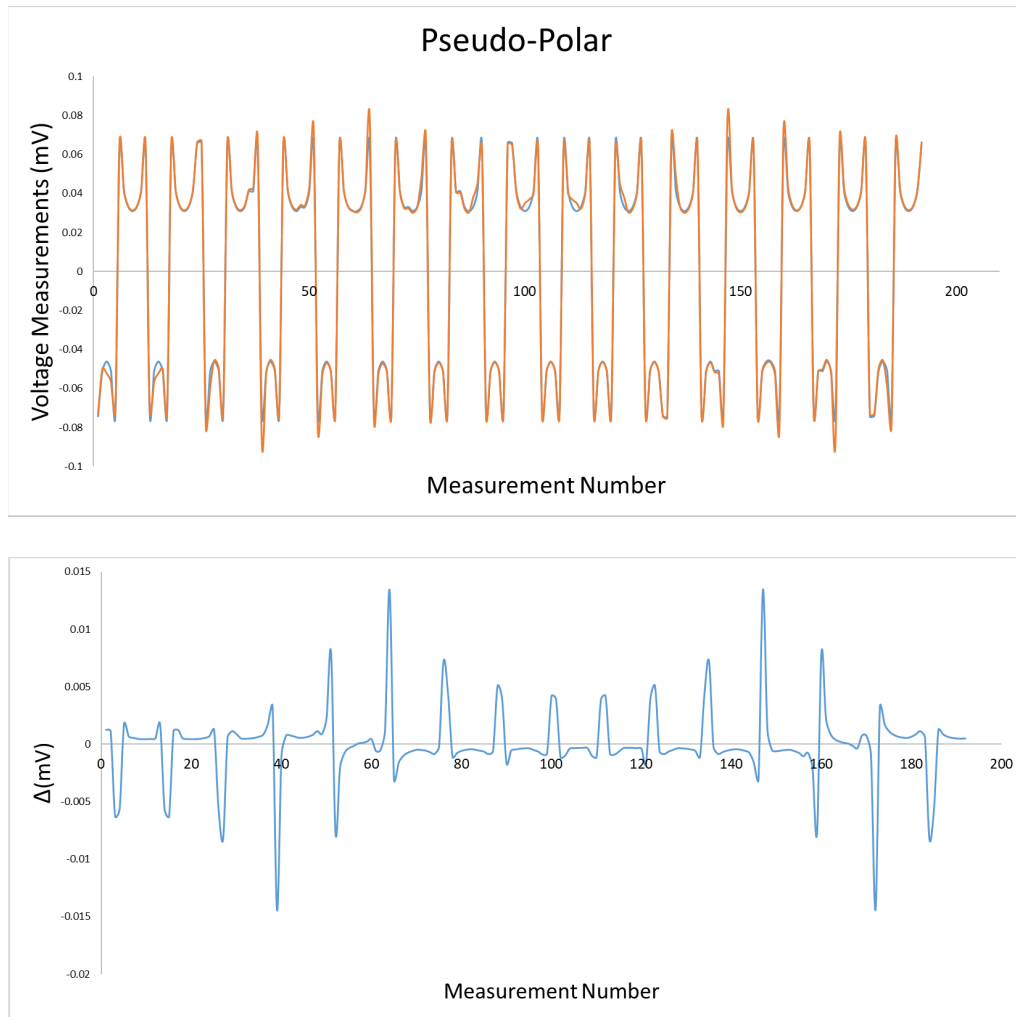
SAVE = sprintf('CRSEC InjElec=%g-Hyp=%g.tif',INJ_PATT(1,2),HYP);
saveas(CRSEC,SAVE);

SAVE = sprintf('CRSEC FWHM InjElec=%g-Hyp=%g.tif',INJ_PATT(1,2),HYP);
saveas(CRSEC_FWHM,SAVE);

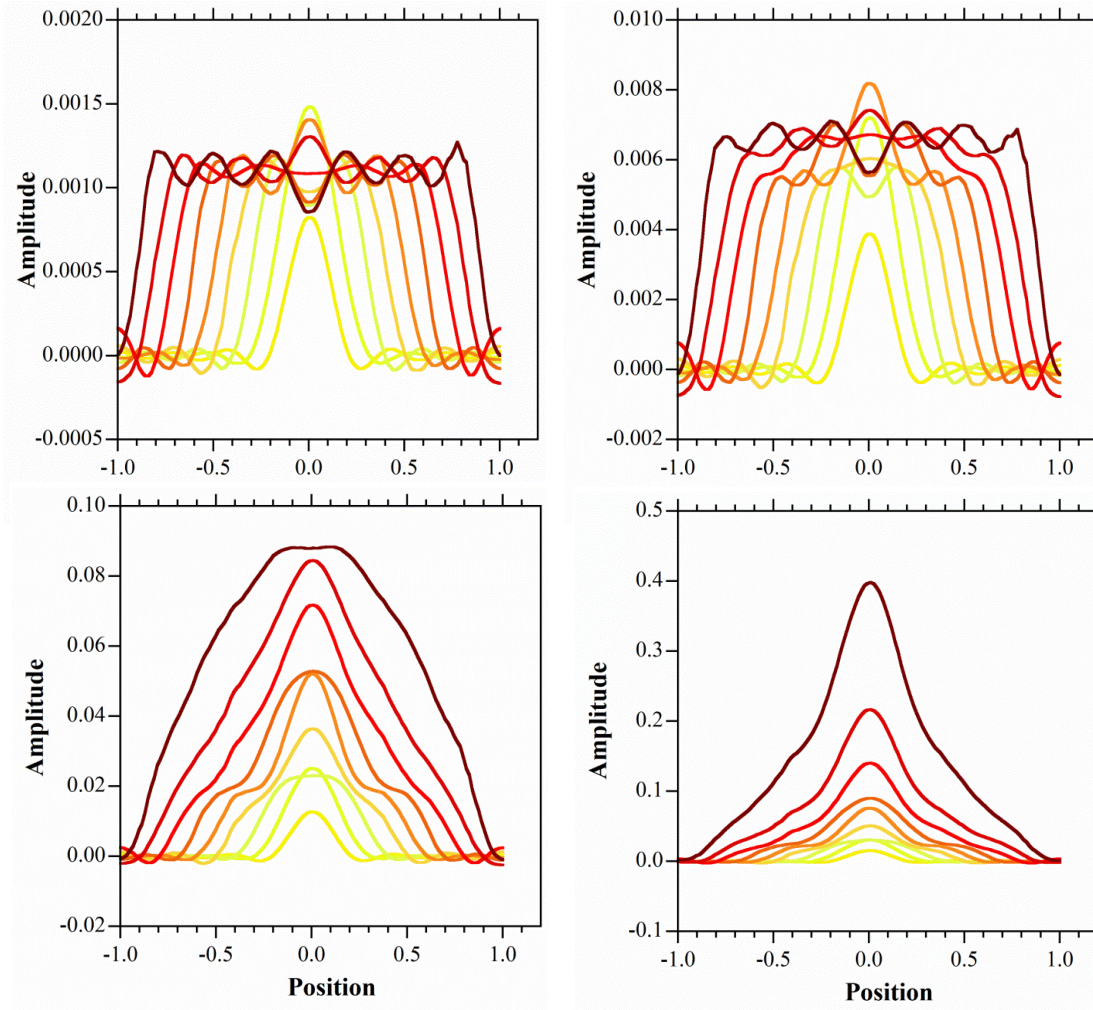
% max(BASE_VOLT.volt(:,:))
% max(BASE_VOLT.meas)

```

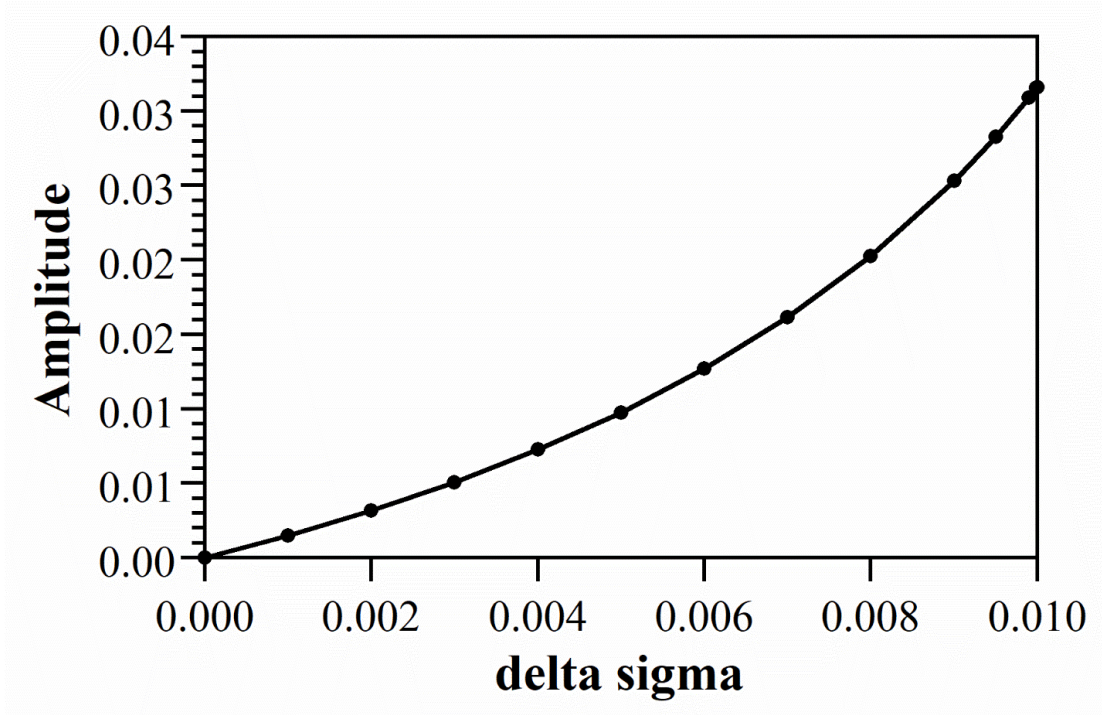
## Appendix B: Supporting Information for Chapter 2



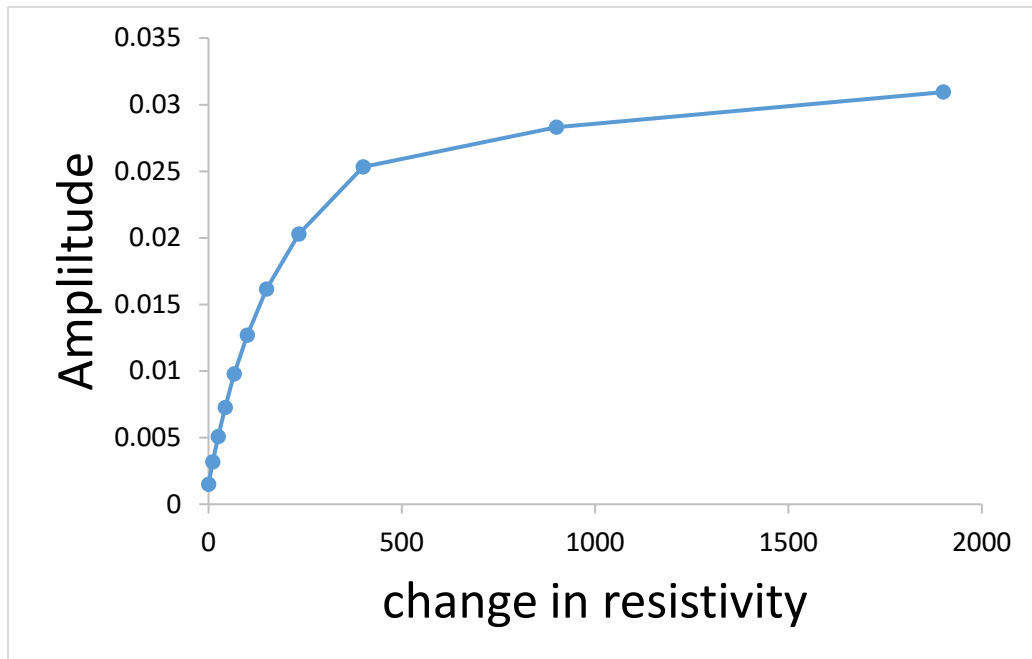
**B 1 TOP:** Boundary potentials  $\vec{V}_{touch}$  and  $\vec{V}_{ref}$  resulting from PP with (orange) and without (blue) a touch near the perimeter ( $x = 0.7$ ), respectively. **BOTTOM:** The signal  $\Delta = \vec{V}_{touch} - \vec{V}_{ref}$ . Note the negative values.



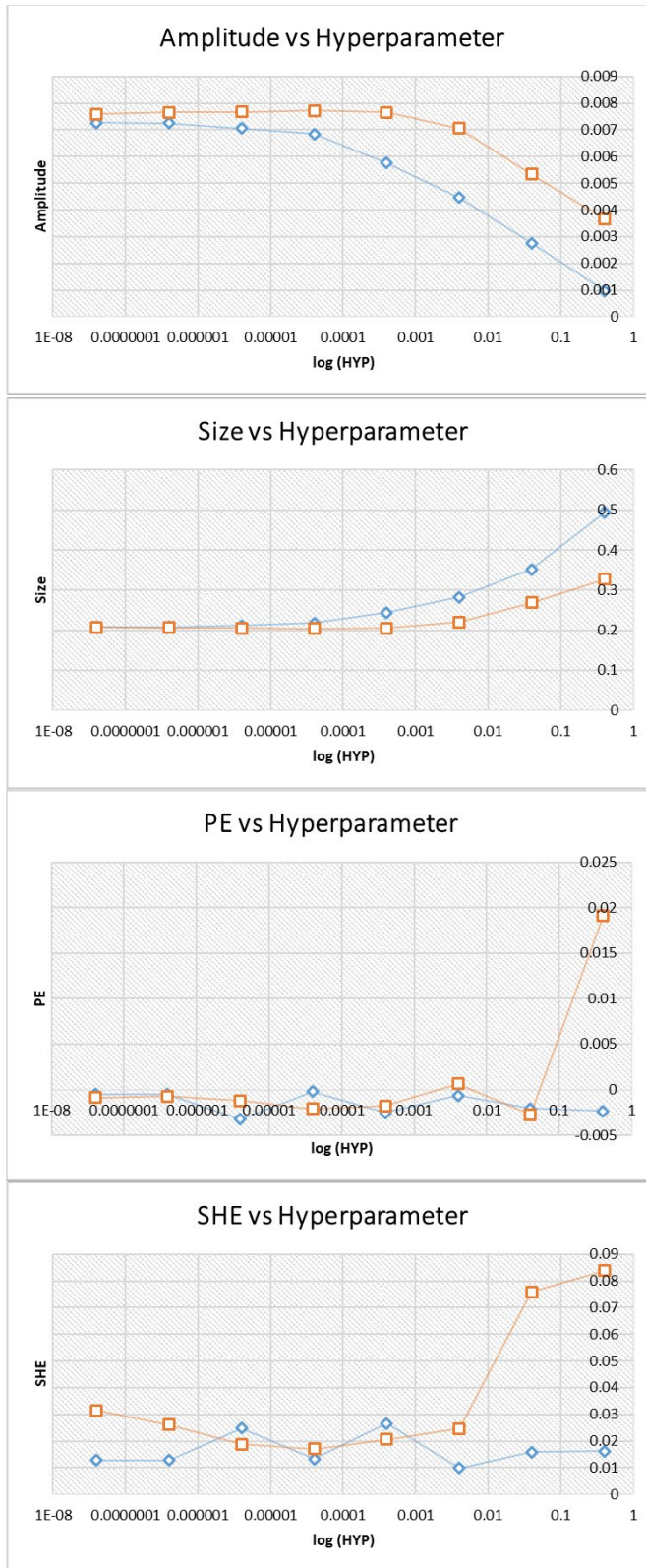
**B 2** Cross-section profiles with different targets sizes (from  $r_t = 0.2$  to  $0.9$ ) with  $\Delta\sigma = 0.001$  (top left),  $\Delta\sigma = 0.004$  (top right),  $\Delta\sigma = 0.009$  (bottom left),  $\Delta\sigma = 0.0099$  S/m (bottom right).



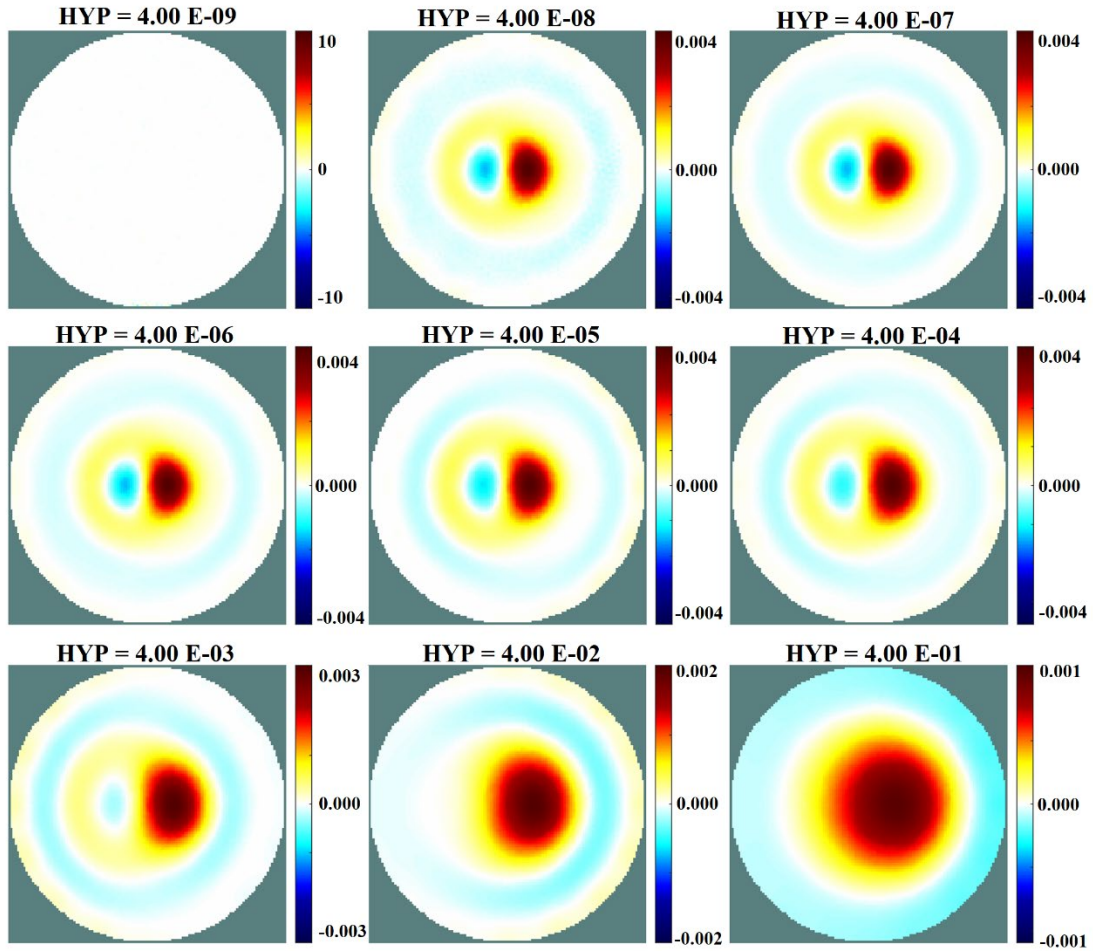
**B 3 Amplitude as a function of  $\Delta\sigma$  with  $\sigma_0 = 0.01$  S/m**



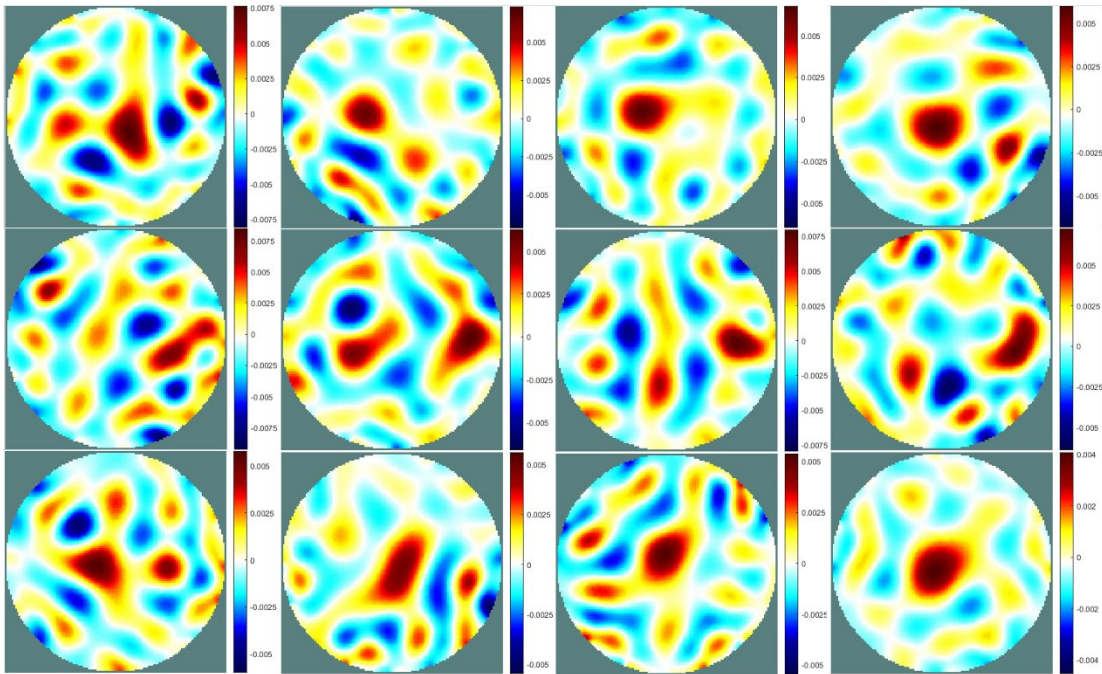
**B 4 Amplitude as a function of change in resistivity with baseline resistivity  $\rho = 100$  ohm-m ( $\sigma = 0.01$  S/m).**



**B 5 Hyperparameter vs (a) Amplitude (b) Reconstructed size (c) Position Error (d) Shape error with target at  $x = 0$  (blue) and  $x = 0.7$  (orange).**



**B 6** Reconstructed EIT images with polar injection pattern with different hyperparameter. Reconstruction failed below  $\lambda=4 \times 10^{-8}$ . Note change in scale with different hyperparameter.



**B 7 (Top row) Reconstructed images for a target at  $x = 0$  and  $x = 0.7$  (Center row) with  $3 \times 10^{-4}$  V with a hyperparameter of  $\lambda = 2 \times 10^{-2}$  for adjacent injection. (Bottom row) Reconstructed images for a target at  $x = 0$  with  $3 \times 10^{-4}$  V with a hyperparameter of  $\lambda = 2 \times 10^{-2}$  pseudo polar injection.**

## Bibliography

1. D.S. Holder and B.H. Brown, *Biomedical Applications of Eit - a Critical-Review*. Clinical and Physiological Applications of Electrical Impedance Tomography, 1993: p. 6-40.
2. D.S. Holder, *Electrical impedance tomography: methods, history, and applications*. Medical physics and biomedical engineering, ed. C.G. Orton, J.H. Nagel, and J.G. Webster. 2005, Bristol, UK: Institute of Physics Publishing.
3. B.S. Kim, G. Boverman, J.C. Newell, G.J. Saulnier, and D. Isaacson, *The complete electrode model for EIT in a mammography geometry*. Physiological Measurement, 2007. **28**(7): p. S57-S69.
4. Y. Chen, *Tactile sensing with compliant structures for human-robot interaction*, in *Department of Mechanical Engineering 2018*, University of Maryland.
5. D.S. Tawil, D. Rye, and M. Velonaki, *Interpretation of the modality of touch on an artificial arm covered with an EIT-based sensitive skin*. Int. J. Robot. Res., 2012. **31**(13): p. 1627-1641.
6. D.S. Tawil, D. Rye, M. Soleimani, and M. Velonaki, *Electrical impedance tomography for artificial sensitive robotic skin: a review*. IEEE Sensors J., 2015. **15**(4): p. 2016.
7. W.X. Ruan, R. Guardo, and A. Adler, *Experimental evaluation of two iterative reconstruction methods for induced current electrical impedance tomography*. IEEE T. Med. Imaging, 1996. **15**(2): p. 180-187.

8. A. Borsic, B.M. Graham, A. Adler, and W.R.B. Lionheart, *In vivo impedance imaging with total variation regularization*. Ieee T. Med. Imaging, 2010. **29**(1): p. 44-54.
9. B. Brandstatter, *Jacobian calculation for electrical impedance tomography based on the reciprocity principle*. IEEE Trans. Magn., 2003. **39**(3): p. 1309-1312.
10. M. Cheney and D. Isaacson, *NOSER: An algorithm for solving the inverse conductivity problem*. Int. J. Imaging Syst. Technol., 1990. **2**: p. 66-75.
11. W.R.B. Lionheart, *EIT reconstruction algorithms: pitfalls, challenges and recent developments*. Physiol. Meas., 2004. **25**(1): p. 125-142.
12. A. Nagakubo, H. Alirezaei, and Y. Kuniyoshi. *A deformable and deformation sensitive tactile distribution sensor*. in *IEEE Int'l Conf. on Robotics and Biomimetics (ROBIO)*. 2007. Sanya, China.
13. Y. Chen, M. Yu, H.A. Bruck, and E. Smela, *Compliant multi-layer tactile sensing for enhanced identification of human touch*. Smart Mater. Struct., 2018. **27**(12).
14. A. Adler and W.R.B. Lionheart, *Uses and abuses of EIDORS: an extensible software base for EIT*. Physiol. Meas., 2006. **27**(5): p. S25-42.
15. A. Adler, J.H. Arnold, R. Bayford, A. Borsic, B. Brown, P. Dixon, T.J.C. Faes, I. Frerichs, H. Gagnon, Y. Garber, B. Grychtol, G. Hahn, W.R.B. Lionheart, A. Malik, R.P. Patterson, J. Stocks, A. Tizzard, N. Weiler, and G.K. Wolf, *GREIT: a unified approach to 2D linear EIT reconstruction of lung images*. Physiol. Meas., 2009. **30**(6): p. S35-S55.

16. N. Polydorides and W.R.B. Lionheart, *A Matlab toolkit for three-dimensional electrical impedance tomography: a contribution to the Electrical Impedance and Diffuse Optical Reconstruction Software project*. Meas. Sci. Technol., 2002. **13**: p. 1871-1883.
17. T. Tallman, S. Gungor, K. Wang, and C. Bakis, *Tactile imaging and distributed strain sensing in highly flexible carbon nanofiber/polyurethane nanocomposites*. Carbon, 2015. **95**: p. 485-493.
18. S.R. Aw, R.A. Rahim, M.H.F. Rahiman, F.R.M. Yunus, and C.L. Goh, *Electrical resistance tomography: A review of the application of conducting vessel walls*. Powder Technol., 2014. **254**: p. 256-264.
19. F. Dickin and M. Wang, *Electrical resistance tomography for process applications*. Meas. Sci. Technol., 1996. **7**(3): p. 247-260.
20. H. Alirezaei, A. Nagakubo, and Y. Kuniyoshi. *A highly stretchable tactile distribution sensor for smooth surfaced humanoids*. in *IEEE/RAS Int'l. Conf. on Humanoid Robots*. 2007. Pittsburgh, PA.
21. D.B. Geselowitz, *An application of electrocardiographic lead theory to impedance plethysmography*. IEEE Trans. Biomed. Eng., 1971. **BME-18**(1): p. 38-41.
22. S. Russo, S. Nefti-Meziani, N. Carbonaro, and A. Tognetti, *A quantitative evaluation of drive pattern selection for optimizing EIT-based stretchable sensors*. Sensors, 2017. **17**(9): p. 1999.
23. A. Adler, P.O. Gaggero, and Y. Maimaitijiang, *Adjacent stimulation and measurement patterns considered harmful*. Physiol. Meas., 2011. **32**(7).

24. X.T. Shi, X.Z. Dong, W.J. Shuai, F.S. You, F. Fu, and R.G. Liu, *Pseudo-polar drive patterns for brain electrical impedance tomography*. *Physiol. Meas.*, 2006. **27**(11): p. 1071-1080.
25. A. Adler. *Strange effect: opposite vs adjacent measurement/stimulation*. 2017 Feb 28, 2017 [cited 2019; Available from: [eidors3d.sourceforge.net/tutorial/strange\\_effects/opposite\\_meas.shtml](http://eidors3d.sourceforge.net/tutorial/strange_effects/opposite_meas.shtml)].
26. J.G. Webster, *Electrical impedance tomography*. The Adam Hilger series on biomedical engineering. 1990, Bristol, England ; New York, NY: Hilger. xii, 224 p.
27. B.M. Graham and A. Adler, *Objective selection of hyperparameter for EIT*. *Physiol. Meas.*, 2006. **27**(5): p. S65-S79.
28. M. Wang, Q. Wang, and B. Karki, *Arts of electrical impedance tomographic sensing*. *Philosophical Transactions of the Royal Society a-Mathematical Physical and Engineering Sciences*, 2016. **374**(2070).